

High-order implicit shock tracking boundary conditions for flows with parametrized shocks

Tianci Huang^{a,1}, Charles Naudet^{a,2}, Matthew J. Zahr^{a,3,*}

^a*Department of Aerospace and Mechanical Engineering, University of Notre Dame, Notre Dame, IN 46556, United States*

Abstract

High-order implicit shock tracking (fitting) is a class of high-order, optimization-based numerical methods to approximate solutions of conservation laws with non-smooth features by aligning elements of the computational mesh with non-smooth features. This ensures the non-smooth features are perfectly represented by inter-element jumps and high-order basis functions approximate smooth regions of the solution without nonlinear stabilization, which leads to accurate approximations on traditionally coarse meshes. In this work, we introduce a robust implicit shock tracking framework specialized for problems with parameter-dependent lead shocks (i.e., shocks separating a farfield condition from the downstream flow), which commonly arise in high-speed aerodynamics and astrophysics applications. After a shock-aligned mesh is produced at one parameter configuration, all elements upstream of the lead shock are removed and the nodes on the lead shock are positioned for new parameter configurations using the implicit shock tracking solver. The proposed framework can be used for most many-query applications involving parametrized lead shocks such as optimization, uncertainty quantification, parameter sweeps, “what-if” scenarios, or parameter-based continuation. We demonstrate the robustness and flexibility of the framework using a one-dimensional space-time Riemann problem, and two- and three-dimensional supersonic and hypersonic benchmark problems.

Keywords: Shock fitting, high-order methods, discontinuous Galerkin, bow shocks, many-query analysis, hypersonics

1. Introduction

Bow shocks are strong, detached, curved shocks that frequently arise in aerospace and astrophysics applications. The strength, geometry, and stand-off distance of bow shocks are highly dependent on the problem configuration including farfield conditions, the geometry of the body, and fluid properties. As the flow speed increases, accurate resolution of the lead shock in a computational setting is paramount to predict quantities of interest integrated over the body, particularly aerodynamic heating [19, 6]. This has forced computational fluid dynamics researchers and practitioners to invest substantial effort and resources to generate hexahedral meshes with very tight grid spacing near shocks and elements aligned to the curvature of the lead shock [29, 19, 5, 20, 7]. Given the substantial amount of user-intensive effort [19, 5] required to mesh and simulate a single configuration, *many-query* analyses such as optimization, uncertainty quantification, parameter sweeps, “what-if” scenarios, or even parameter-based continuation, remain a significant challenge because they cause the bow shock to move, which requires modifications to the mesh.

Shock capturing is a popular and effective class of approaches to stabilize higher-than-first-order methods in the vicinity of shocks on a fixed computational grid. Limiters, which are used to limit the solution gradient near shocks, are commonly used with second-order finite volume methods [37] and high-order discontinuous Galerkin (DG) methods [11]. These methods are commonly used in real-world flow simulations; however, they place stringent demands on the computational mesh for high-speed flows (hexahedral elements, tight

*Corresponding author

Email addresses: thuang5@nd.edu (Tianci Huang), cnaudet@nd.edu (Charles Naudet), mzahr@nd.edu (Matthew J. Zahr)

¹Graduate Student, Department of Aerospace and Mechanical Engineering, University of Notre Dame

²Graduate Student, Department of Aerospace and Mechanical Engineering, University of Notre Dame

³Assistant Professor, Department of Aerospace and Mechanical Engineering, University of Notre Dame

grid spacing near shocks, alignment of elements with lead shock) [7] and are not well-suited for many-query studies involving parametrized shocks. Weighted essentially non-oscillatory (WENO) methods [21, 30, 24] use stencil-based high-order reconstruction near shocks to mitigate spurious oscillations and can lead to crisp shocks on structured meshes. They have shown good agreement with experiments for high-speed flows [35, 28], although they are not well-suited for complex domains that require unstructured meshes. For high-order methods, artificial viscosity approaches can smoothly resolve steep gradients with sub-cell accuracy and is the preferred shock capturing approach for finite-element-based methods [33, 2, 17, 8]. The combination of high-order DG methods with artificial viscosity has even been shown to reduce the sensitivity of hypersonic flow simulations to the choice of numerical flux and grid alignment [8]. However, artificial viscosity models usually suffer from a relatively strong dependence on a large amount of empirical parameters that must be tuned [39] and require substantial grid refinement near shocks where accuracy has been dropped to first order. As such, these methods are not ideally suited for many-query analyses involving parametrized shocks.

An alternative approach is *shock tracking* or *shock fitting*, where the computational mesh is moved to align faces of mesh elements with solution discontinuities to represent them geometrically with the inter-element jump in the solution basis without requiring additional stabilization. This leads to accurate solutions on coarse meshes when using high-order methods and avoids instabilities often associated with shock capturing methods such as carbuncles. The traditional approach to shock tracking [31, 34] largely consists of explicitly identifying shock locations and using the Rankine-Hugoniot conditions to determine the shock motion and states across the shock. Although research in this area has experienced a resurgence in recent years [9, 3, 18, 16, 1, 43, 10, 4], these methods are most suited for flows with relatively simple shock geometries because they require explicit meshing of the shocks and specialized strategies to track the shocks separately from the remainder of the flow.

A different approach to shock tracking known as *implicit shock tracking*, which includes the High-Order Implicit Shock Tracking (HOIST) method [40, 42, 41] and the Moving Discontinuous Galerkin Method with Interface Condition Enforcement (MDG-ICE) [14, 25, 26], has overcome some of the challenges of traditional approaches to shock tracking. These methods discretize the conservation law on a shock-agnostic mesh and pose an optimization problem whose solution is the discontinuity-aligned mesh and corresponding discretized flow solution. That is, shock tracking is achieved implicitly through the solution of an optimization problem. The meshing challenge from traditional shock tracking approaches is largely circumvented, which leads to a general approach that is independent of the underlying conservation law. These methods have been shown to reliably and effectively solve inviscid and viscous, steady and unsteady, inert and reacting flows of varying degrees of shock complexity [14, 41, 36, 23, 12, 15, 13]. Because these methods inherently and automatically align the computational grid with shocks in the domain, they are well-suited to many-query studies involving parametrized shocks.

We propose a novel framework based on implicit shock tracking, specifically the HOIST method, to efficiently and robustly conduct many-query analyses of problems involving parameter-dependent *lead shocks*. We define a lead shock as a shock (or, more generally, any non-smooth feature) separating the boundary state from the downstream flow. Bow shocks and primary blast waves are examples of lead shocks; however, in the current setting, even the head of a rarefaction wave in a shock tube qualifies. The approach is initialized by applying the HOIST method on a shock-agnostic mesh at one parameter configuration of interest to generate a shock-aligned mesh and the corresponding flow field. Because the grid is aligned with the lead shock, the solution in all elements upstream of the shock will be a constant equal to the boundary state. As such, all elements upstream of the shock are removed to produce a reduced mesh that will be used for all subsequent parameter configurations, with the farfield boundary condition directly applied on the new shock boundary. In our numerical experiments, this can reduce the size of the computational mesh by three-fold, which is additional computational savings on top of the coarse meshes required by implicit shock tracking approaches [23].

With only the portion of the domain downstream of the lead shock modeled, there is no reason to directly optimize for all nodal coordinates in the mesh if the lead shock is the only non-smooth feature in the domain. Instead, we only optimize the positions of the nodes on the shock boundary with all other nodal coordinates determined by boundary constraints and partial differential equation (PDE) based smoothing using the approach in [22]. For problems with secondary non-smooth features in addition to the lead shock, all downstream nodal positions are optimized to eliminate the need for nonlinear stabilization and provide highly accurate solutions. In addition to substantially reducing the overall degrees of freedom (DoFs) of the

implicit shock tracking discretization, it also improves robustness and accelerates convergence because the overall tracking problem is easier and a high-quality initial guess is provided from the solution at previous parameter configurations. The proposed framework can be used for most *many-query* applications involving parametrized lead shocks such as optimization, uncertainty quantification, parameter sweeps, “what-if” scenarios, or parameter-based continuation. In the continuation setting, we outline and demonstrate a procedure to leverage partially converged solves at intermediate stages to improve the efficiency of the approach.

The remainder of the paper is organized as follows. Section 2 introduces the governing system of inviscid conservation laws, its reformulation on a fixed reference domain, and its discretization using a discontinuous Galerkin method. Section 3 provides a brief summary of the HOIST formulation with targeted mesh optimization proposed in [42, 23, 22]. Section 4 introduces the specialized HOIST solver for abstract many-query problems involving parametrized shocks and its specialization to parameter-based continuation with partially converged intermediate stages. Finally, Section 5 demonstrates the robustness and flexibility of the proposed approach for Mach continuation of two- and three-dimensional supersonic and hypersonic problems, and for a parameter sweep of a Riemann problem (Euler equations) parametrized by its initial condition.

2. Governing equations and high-order discretization

In this section, we introduce a system of steady conservation laws whose solution will be assumed to contain a lead shock (Section 2.1). Next, we transform the system of conservation laws to a reference domain such that domain deformations appear explicitly in the governing equations (Section 2.2), and discretize the transformed equations using a high-order DG method (Section 2.3).

2.1. System of conservation laws

Consider a general system of m inviscid conservation laws over $\Omega \subset \mathbb{R}^d$

$$\nabla \cdot F(U) = S(U) \quad \text{in } \Omega, \quad (1)$$

where $U : \Omega \rightarrow \mathbb{R}^m$ is implicitly defined as the solution of (1), $F : \mathbb{R}^m \rightarrow \mathbb{R}^{m \times d}$ is the flux function, and $S : \mathbb{R}^m \rightarrow \mathbb{R}^m$ is the source term. In general, the solution $U(x)$ may contain discontinuities, in which case the conservation law (1) holds away from the discontinuities and the Rankine-Hugoniot conditions hold at discontinuities. In this work, we focus on problems containing a *lead shock* and, for concreteness, focus on the compressible Euler equations (Section 5). However, the method developed in this work applies to any conservation law of the form (1) whose solution contains a lead shock.

2.2. Transformed system of conservation laws on a fixed reference domain

Let \mathbb{G} be the collection of diffeomorphisms from a reference domain Ω_0 to the physical domain Ω , i.e., for $\mathcal{G} \in \mathbb{G}$, we have

$$\mathcal{G} : \Omega_0 \rightarrow \Omega, \quad \mathcal{G} : X \mapsto \mathcal{G}(X). \quad (2)$$

Following the approach in [40], for any $\mathcal{G} \in \mathbb{G}$, the conservation law on the physical domain Ω is transformed to a conservation law on the reference domain Ω_0 as

$$\bar{\nabla} \cdot \bar{F}(\bar{U}; G) = \bar{S}(\bar{U}; g) \quad \text{in } \Omega_0, \quad (3)$$

where $\bar{\nabla}$ is the gradient operator on the reference domain, $\bar{U} : \bar{\Omega} \rightarrow \mathbb{R}^m$ is the transformed solution, $\bar{F} : \mathbb{R}^m \times \mathbb{R}^{d \times d} \rightarrow \mathbb{R}^{m \times d}$ is the transformed flux function, $\bar{S} : \mathbb{R}^m \times \mathbb{R} \rightarrow \mathbb{R}^m$ is the transformed source term, and

$$G = \bar{\nabla} \mathcal{G}, \quad g = \det G \quad (4)$$

are the deformation gradient and Jacobian, respectively, of the mapping $\mathcal{G} \in \mathbb{G}$. For any $X \in \Omega_0$, the transformed and physical solution are related as

$$\bar{U}(X) = U(\mathcal{G}(X)), \quad (5)$$

and the transformed flux and source term are defined as

$$\bar{F} : (\bar{W}; \Theta) \mapsto (\det \Theta) F(\bar{W}) \Theta^{-T}, \quad \bar{S} : (\bar{W}; q) \mapsto q S(\bar{W}). \quad (6)$$

2.3. Discontinuous Galerkin discretization of the transformed conservation law

We use a standard nodal discontinuous Galerkin method to discretize the transformed conservation law (3). Let \mathcal{E}_h represent a discretization of the reference domain Ω_0 into non-overlapping, potentially curved, computational elements. The DG trial space of discontinuous piecewise polynomials associated with the mesh \mathcal{E}_h is defined as

$$\mathcal{V}_h^p = \{v \in [L^2(\Omega_0)]^m \mid v|_K \in [\mathcal{P}_p(K)]^m, \forall K \in \mathcal{E}_h\}, \quad (7)$$

where $\mathcal{P}_p(K)$ is the space of polynomial functions of degree at most $p \geq 1$ on the element K . The space of globally continuous piecewise polynomials of degree q associated with the mesh \mathcal{E}_h is defined as

$$\mathcal{W}_h = \{v \in C^0(\Omega_0) \mid v|_K \in \mathcal{P}_q(K), \forall K \in \mathcal{E}_h\}; \quad (8)$$

we discretize the domain mapping ($\mathcal{G} \in \mathbb{G}$) with the corresponding vector-valued space $[\mathcal{W}_h]^d$. Taking the DG test space to be $\mathcal{V}_h^{p'}$, where $p' \geq p$, the DG formulation is: given $\mathcal{G}_h \in [\mathcal{W}_h]^d$, find $\bar{U}_h \in \mathcal{V}_h^p$ such that for all $\bar{\psi}_h \in \mathcal{V}_h^{p'}$, we have

$$\int_{\partial K} \bar{\psi}_h^+ \cdot \bar{\mathcal{H}}(\bar{U}_h^+, \bar{U}_h^-, N_h; \bar{\nabla} \mathcal{G}_h) dS - \int_K \bar{F}(\bar{U}_h; \bar{\nabla} \mathcal{G}_h) : \bar{\nabla} \bar{\psi}_h dV = \int_K \bar{\psi}_h \cdot \bar{S}(\bar{U}_h; \det(\bar{\nabla} \mathcal{G}_h)) dV, \quad (9)$$

where N_h is the unit outward normal to element $K \in \mathcal{E}_h$, \bar{W}_h^+ (\bar{W}_h^-) denotes the interior (exterior) trace of \bar{W}_h to the element K for $\bar{W}_h \in \mathcal{V}_h^s$ (any $s \in \{0, 1, \dots\}$), and $\bar{\mathcal{H}}$ is the numerical flux function associated with the reference inviscid flux \bar{F} ; see [23] for additional details.

After introducing a basis for the test, trial, and domain mapping spaces, the governing DG equations (9) with $p' = p$ reduces to the algebraic residual form

$$\mathbf{r} : \mathbb{R}^{N_u} \times \mathbb{R}^{N_x} \rightarrow \mathbb{R}^{N_u}, \quad \mathbf{r} : (\mathbf{u}, \mathbf{x}) \mapsto \mathbf{r}(\mathbf{u}, \mathbf{x}), \quad (10)$$

where $N_u = \dim \mathcal{V}_h^p$ and $N_x = \dim([\mathcal{W}_h]^d)$; $\mathbf{u} \in \mathbb{R}^{N_u}$ is the vector of flow field coefficients and $\mathbf{x} \in \mathbb{R}^{N_x}$ is the vector of nodal coordinates of the mesh (also called mesh DoFs). Notice that for a fixed mesh \mathbf{x} , (10) is a standard DG discretization residual. In addition, we define the algebraic enriched residual associated with a test space of degree $p' = p + 1$ as

$$\mathbf{R} : \mathbb{R}^{N_u} \times \mathbb{R}^{N_x} \rightarrow \mathbb{R}^{N'_u}, \quad \mathbf{R} : (\mathbf{u}, \mathbf{x}) \mapsto \mathbf{R}(\mathbf{u}, \mathbf{x}), \quad (11)$$

where $N'_u = \dim \mathcal{V}_h^{p'}$, which will later be used to construct the HOIST objective function.

3. The High-Order Implicit Shock Tracking (HOIST) method

In this section, we provide a brief summary of the HOIST method with targeted mesh optimization [42, 23], which allows only a selected portion of the mesh DoFs to be optimized while aligning mesh faces with non-smooth solution features and preserving boundaries. This is achieved by partitioning the mesh DoFs $\mathbf{x} \in \mathbb{R}^{N_x}$ as

$$\mathbf{x} = (\mathbf{x}_c, \mathbf{x}_u), \quad \mathbf{x}_u = (\mathbf{y}, \mathbf{x}_s) \quad (12)$$

where $\mathbf{x}_c \in \mathbb{R}^{N_c}$ are the constrained DoFs and $\mathbf{x}_u \in \mathbb{R}^{N_u}$ are the unconstrained DoFs. Following [23], \mathbf{x}_u can be freely chosen (e.g., to align element faces with non-smooth features), whereas \mathbf{x}_c is uniquely determined from \mathbf{x}_u . Following [22], unconstrained DoFs are further partitioned into optimized DoFs $\mathbf{y} \in \mathbb{R}^{N_y}$ and smoothed DoFs $\mathbf{x}_s \in \mathbb{R}^{N_s}$, where \mathbf{y} will be optimized for shock alignment and \mathbf{x}_s will be determined through PDE-based smoothing. For abstraction, we let ϕ be a parametrization of the mesh DoFs

$$\phi : \mathbb{R}^{N_y} \rightarrow \mathbb{R}^{N_x}, \quad \phi : \mathbf{y} \mapsto \phi(\mathbf{y}), \quad (13)$$

that maps the optimized mesh DoFs to all mesh DoFs, i.e., $\mathbf{x} = \phi(\mathbf{y})$. The parametrization must be constructed to ensure 1) optimized mesh DoFs (\mathbf{y}) can move freely, 2) nodes on fixed domain boundaries can only slide along those boundaries by computing the constrained mesh DoFs (\mathbf{x}_c) from \mathbf{y} , and 3) smoothed mesh DoFs (\mathbf{x}_s) are determined through PDE-based smoothing (e.g., linear elasticity equations with pure Dirichlet boundary conditions). A complete description of the construction of ϕ can be found in [42, 23] (boundary preservation only) and [22] (boundary preservation and PDE-based smoothing).

The HOIST method is formulated as an optimization problem over the DG solution coefficients and the optimized mesh DoFs as

$$(\mathbf{u}^*, \mathbf{y}^*) := \arg \min_{\mathbf{u} \in \mathbb{R}^{N_u}, \mathbf{y} \in \mathbb{R}^{N_y}} f(\mathbf{u}, \phi(\mathbf{y})) \quad \text{subject to: } \mathbf{r}(\mathbf{u}, \phi(\mathbf{y})) = \mathbf{0}, \quad (14)$$

where $f : \mathbb{R}^{N_u} \times \mathbb{R}^{N_x} \rightarrow \mathbb{R}$ is the objective function defined in [42, 23] and $\mathbf{x}^* = \phi(\mathbf{y}^*)$ are the nodal coordinates of the discontinuity-aligned mesh. The objective function consists of two terms as

$$f : (\mathbf{u}, \mathbf{x}) \mapsto f_{\text{err}}(\mathbf{u}, \mathbf{x}) + \kappa^2 f_{\text{msh}}(\mathbf{x}), \quad (15)$$

where $f_{\text{err}} : \mathbb{R}^{N_u} \times \mathbb{R}^{N_x} \rightarrow \mathbb{R}$ is the alignment term and $f_{\text{msh}} : \mathbb{R}^{N_x} \rightarrow \mathbb{R}$ is a mesh quality term, defined as

$$f_{\text{err}} : (\mathbf{u}, \mathbf{x}) \mapsto \frac{1}{2} \|\mathbf{R}(\mathbf{u}, \mathbf{x})\|_2^2, \quad f_{\text{msh}} : \mathbf{x} \mapsto \frac{1}{2} \|\mathbf{R}_{\text{msh}}(\mathbf{x})\|_2^2, \quad (16)$$

$\mathbf{R}_{\text{msh}} : \mathbb{R}^{N_x} \rightarrow \mathbb{R}^{|\mathcal{E}_h|}$ is an element-wise mesh distortion residual defined in [23], and κ is a penalty parameter that balances the alignment and mesh quality objectives; see [23] for a complete definition of \mathbf{R}_{msh} and an adaptive algorithm to set κ . The norm of the enriched DG residual has proven to be an effective alignment indicator [42, 23] because it penalizes non-physical oscillations that will arise on meshes that do not fit solution discontinuities.

A sequential quadratic programming (SQP) method with a modified Levenberg-Marquardt Hessian approximation introduced in [14, 42] is used to solve the optimization problem (14). The SQP solver simultaneously converges the optimized mesh DoFs (\mathbf{y}) and the DG solution coefficients (\mathbf{u}) to their optimal values, i.e., a high-order DG solution (\mathbf{u}^*) on a discontinuity-aligned mesh ($\phi(\mathbf{y}^*)$). This is accomplished by combining the solution and optimized mesh DoFs into a single vector of optimization variables $\mathbf{z} = (\mathbf{u}, \mathbf{y}) \in \mathbb{R}^{N_z}$ ($N_z = N_u + N_y$) and generating a sequence of iterates as

$$\mathbf{z}_{i+1} = \mathbf{z}_i + \alpha_i \Delta \mathbf{z}_i \quad (17)$$

for $i = 0, 1, \dots$, where $\mathbf{z}_i \in \mathbb{R}^{N_z}$ is the vector of optimization variables at iteration i , $\Delta \mathbf{z}_i \in \mathbb{R}^{N_z}$ is the search direction at the i th iteration, and $\alpha_i \in \mathbb{R}_{>0}$ is the step length at the i th iteration. The search direction is determined at each iteration by solving a quadratic approximation to (14) at \mathbf{z}_i and the step length is determined via a line search of an ℓ_1 merit function. A complete description of the HOIST method and solver can be found in [42, 23].

4. The HOIST method for flows with parametrized shocks

In this section, we introduce a framework for solving flows with parametrized lead shocks using the HOIST method. This approach can be leveraged for *many-query* analyses such as optimization, uncertainty quantification, parameter sweeps, or “what-if” scenarios, or to drive a continuation strategy for more complex flow regimes.

4.1. Parametrized setting

While not introduced as such for brevity, all terms in the conservation law (1) as well as its transformed (3) and discrete variants (10)-(11) depend on *problem data* such as boundary condition, domain geometry, material properties, etc. Many-query analyses and continuation-based solvers inherently vary one or more of these parameters for some purpose, e.g., find an optimal solution (optimization), compute a probability

distribution (uncertainty quantification), solve a complex problem using a sequence of easier ones (continuation). To handle these settings, we explicitly introduce dependence of the discretized residuals on a collection of parameters. That is, we redefine the standard DG residual in (10) as

$$\mathbf{r} : \mathbb{R}^{N_u} \times \mathbb{R}^{N_x} \times \mathcal{D} \rightarrow \mathbb{R}^{N_u}, \quad \mathbf{r} : (\mathbf{u}, \mathbf{x}; \boldsymbol{\mu}) \mapsto \mathbf{r}(\mathbf{u}, \mathbf{x}; \boldsymbol{\mu}) \quad (18)$$

and the enriched DG residual in (11) as

$$\mathbf{R} : \mathbb{R}^{N_u} \times \mathbb{R}^{N_x} \times \mathcal{D} \rightarrow \mathbb{R}^{N'_u}, \quad \mathbf{R} : (\mathbf{u}, \mathbf{x}; \boldsymbol{\mu}) \mapsto \mathbf{R}(\mathbf{u}, \mathbf{x}; \boldsymbol{\mu}), \quad (19)$$

where $\mathcal{D} \subset \mathbb{R}^{N_\mu}$ is a space of admissible parameter configurations and $\boldsymbol{\mu} \in \mathcal{D}$ is a vector of parameters that either directly or indirectly defines relevant problem data. For this work, we assume that for any $\boldsymbol{\mu} \in \mathcal{D}$, the flow contains a lead shock that separates the farfield from shock-downstream portion of the domain. Furthermore, we assume topologically equivalent or similar lead shocks for all $\boldsymbol{\mu} \in \mathcal{D}$.

From these definitions, the HOIST solution in (14) becomes parameter dependent, and we let $(\mathbf{u}_\mu^*, \mathbf{y}_\mu^*) \subset \mathbb{R}^{N_u} \times \mathbb{R}^{N_y}$ denote the solutions of (14) with \mathbf{r} and \mathbf{R} replaced by $\mathbf{r}(\cdot, \cdot; \boldsymbol{\mu})$ and $\mathbf{R}(\cdot, \cdot; \boldsymbol{\mu})$, respectively. Because the optimization problem in (14) is non-convex, it will have multiple local minima. However, from a given starting point $(\bar{\mathbf{u}}, \bar{\mathbf{y}})$, the HOIST solver [23] will return a single solution. We let $\Upsilon : \mathbb{R}^{N_u} \times \mathbb{R}^{N_y} \times \mathcal{D} \rightarrow \mathbb{R}^{N_u} \times \mathbb{R}^{N_y}$ be an operator that maps the starting point $(\bar{\mathbf{u}}, \bar{\mathbf{y}})$ and parameter configuration $\boldsymbol{\mu}$ to the element of the set $(\mathbf{u}_\mu^*, \mathbf{y}_\mu^*)$ returned by the HOIST solver, i.e.,

$$\Upsilon : (\bar{\mathbf{u}}, \bar{\mathbf{y}}, \boldsymbol{\mu}) \mapsto \Upsilon(\bar{\mathbf{u}}, \bar{\mathbf{y}}, \boldsymbol{\mu}) \in (\mathbf{u}_\mu^*, \mathbf{y}_\mu^*). \quad (20)$$

4.2. Many-query analysis

In the remainder, we consider an abstract many-query setting where our goal is to determine the solution of the conservation law for all parameter configurations in an ordered subset $\Xi \subset \mathcal{D}$ with $\Xi = \{\boldsymbol{\mu}_1, \dots, \boldsymbol{\mu}_N\}$. Depending on the many-query setting, the set may be known *a priori* (e.g., parameter sweeps, static continuation, Monte Carlo approaches to uncertainty quantification), or built adaptively (e.g., optimization, adaptive continuation, “what-if” scenarios). The solutions of the conservation law will be computed sequentially according to the ordering of the parameters, where the initial guess for the flow and mesh DoFs will come from the solution of the previous parameter. Optimal ordering of the parameters will depend on the many-query setting and the problem under consideration.

For the first parameter $\boldsymbol{\mu}_1$, we follow the standard HOIST approach (no PDE-based smoothing) [23] where the initial mesh DoFs ($\bar{\mathbf{y}}$) come directly from a mesh generator and the initial flow solution ($\bar{\mathbf{u}}$) is the first-order finite volume solution of the parametrized PDE at $\boldsymbol{\mu} = \boldsymbol{\mu}_1$ (or any other reasonable initial guess). From this initial guess, we compute the HOIST solution and make the observation that the solution in all elements upstream of the shock is constant and equal to the farfield boundary condition, making this a costly waste of degrees of freedom. Therefore, we remove all elements upstream of the lead shock and directly apply the farfield boundary condition to the lead shock itself (referred to as the *shock boundary* in the remainder). This procedure is illustrated in Figure 1.

For all subsequent parameters, only elements downstream of the lead shock remain so changes to the lead shock position and shape come from deformations to the shock boundary. For problems where the lead shock is the *only* shock for all $\boldsymbol{\mu} \in \mathcal{D}$, we take the optimized mesh DoFs (\mathbf{y}) to be all DoFs on the shock boundary and the smoothed mesh DoFs (\mathbf{x}_s) to be all remaining unconstrained mesh DoFs (Figure 1). In this case, there is no need to allow topological changes to the mesh (e.g., element collapses as in [23]) so the mesh parametrization ϕ will be fixed for all parameters $\boldsymbol{\mu}_2, \dots, \boldsymbol{\mu}_N$. For problems with secondary shocks, all unconstrained mesh DoFs are taken as optimized mesh DoFs. For either case, nodes that lie on the intersection of the lead shock boundary and other boundaries should respect the constraints of the fixed boundaries (Figure 1). In this work, we consider problems with only lead shocks as well as problems with both lead and secondary shocks.

With the initial HOIST solve, element removal, and mesh parametrization settled, we state the many-query analysis algorithm. Let $(\mathbf{u}_1^*, \mathbf{y}_1^*)$ denote the HOIST solution after the elements upstream of the shock have been removed and the nodal coordinates are parametrized on the new mesh. Then, for $k = 2, \dots, N$,

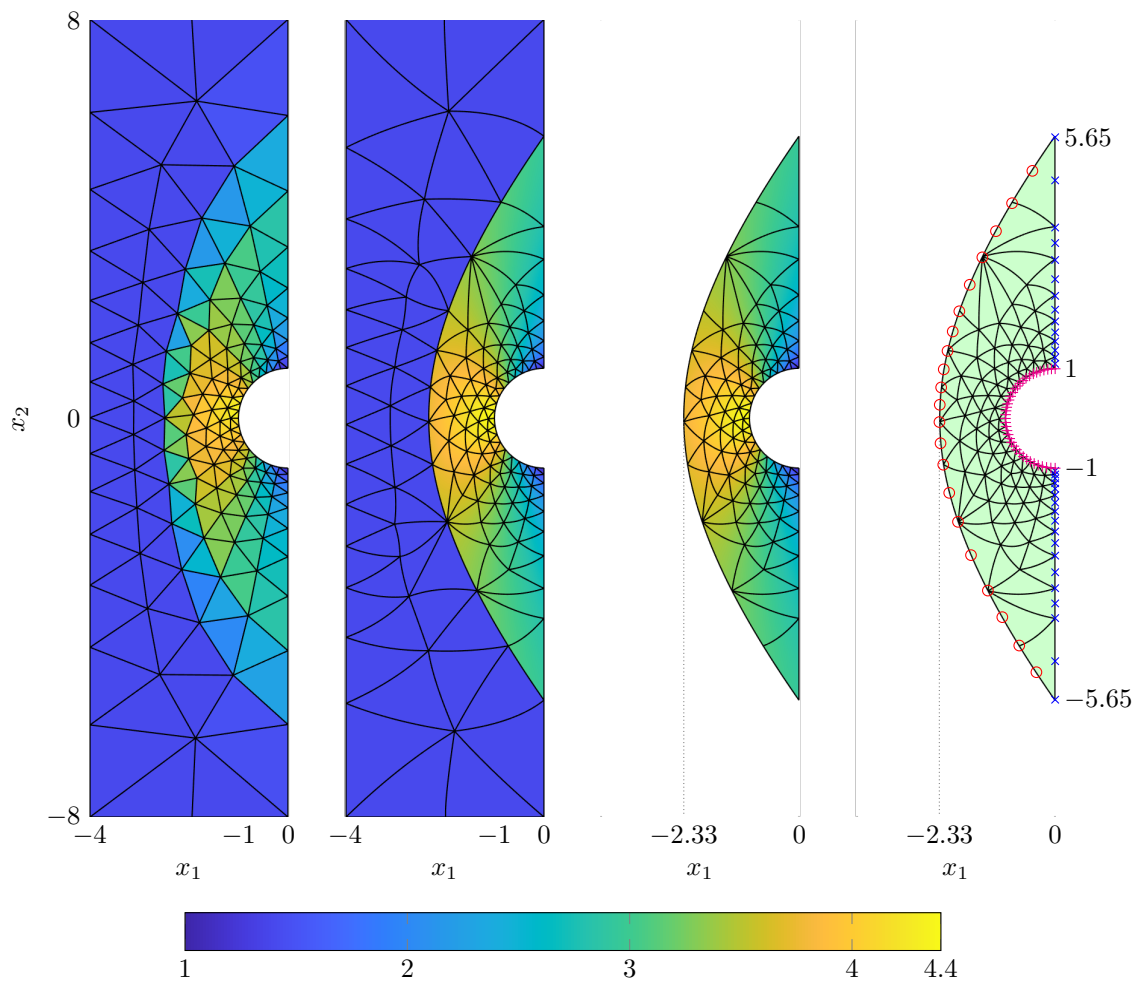


Figure 1: Initial guess (density) on a shock-agnostic mesh of $M_\infty = 2$ flow over cylinder (*left*), the shock-aligned mesh and corresponding solution obtained using HOIST (*middle-left*), the corresponding solution and mesh extracted from downstream the bow shock (*middle-right*), and a schematic visualizing the mesh parametrization (*right*). Legend: shock boundary nodes that move freely (\circ), outlet boundary nodes that are constrained to slide along original boundary (\times), cylinder boundary nodes that are fixed ($+$), and all remaining nodes (not shown for clarity) are determined from PDE-based smoothing.

we define the HOIST solution at parameter $\boldsymbol{\mu}_k$ as

$$(\mathbf{u}_k^*, \mathbf{y}_k^*) := \Upsilon(\mathbf{u}_{k-1}^*, \mathbf{y}_{k-1}^*, \boldsymbol{\mu}_k). \quad (21)$$

That is, the HOIST solution for $\boldsymbol{\mu}_k$ is initialized from the HOIST solution at $\boldsymbol{\mu}_{k-1}$. Because the nodal coordinates are parametrized with optimized mesh DoFs on the lead shock boundary, the HOIST method naturally deforms that boundary to align with the new lead shock location (Section 5). The complete algorithm is summarized in Algorithm 1.

Remark 1. *The number of unconstrained mesh DoFs have been significantly reduced by removing elements upstream of the shock and only including nodes on the lead shock as unconstrained mesh DoFs relative to the standard HOIST setting. This allows the lead shock to be tracked with high accuracy, but can stall deep convergence of the HOIST solver to tight optimality tolerances. Rapid, deep convergence can be restored by terminating the HOIST solver once the mesh has converged and updating \mathbf{u}_k^* with the solution of*

$$\mathbf{r}(\cdot, \phi(\mathbf{y}_k^*); \boldsymbol{\mu}_k) = \mathbf{0} \quad (22)$$

starting from the HOIST output \mathbf{u}_k^* , e.g., using Newton-Raphson iterations. That is, the HOIST flow solution is updated with a fixed-mesh DG solve. Algorithms 1-2 both include this (optional) fixed mesh solve.

Algorithm 1 HOIST method for many-query analysis with parametrized lead shock

Input: Reference mesh of entire domain $\bar{\mathcal{E}}_h$, parameter set $\Xi = \{\boldsymbol{\mu}_1, \dots, \boldsymbol{\mu}_N\}$

Output: HOIST solution over Ξ : $\{(\mathbf{u}_1^*, \mathbf{y}_1^*), \dots, (\mathbf{u}_N^*, \mathbf{y}_N^*)\}$

- 1: **Initial HOIST solve:** Compute HOIST solution $(\bar{\mathbf{u}}_1^*, \bar{\mathbf{y}}_1^*)$ at $\boldsymbol{\mu}_1$ over $\bar{\mathcal{E}}_h$
 - 2: **Reduce mesh:** Create reduced mesh \mathcal{E}_h as $\bar{\mathcal{E}}_h$ without elements upstream of the lead shock
 - 3: **Transfer solution:** Transfer solution $\bar{\mathbf{u}}_1^*$ to reduced mesh \mathbf{u}_1^*
 - 4: **Parametrize reduced mesh:** Determine parametrization of reduced mesh ϕ (Section 4.2)
 - 5: **Transfer mesh DoFs:** Transfer mesh DoFs $\bar{\mathbf{y}}_1^*$ to reduced mesh \mathbf{y}_1^*
 - 6: **for** $k = 2, \dots, N$ **do**
 - 7: **HOIST solve:** $(\mathbf{u}_k^*, \mathbf{y}_k^*) = \Upsilon(\mathbf{u}_{k-1}^*, \mathbf{y}_{k-1}^*, \boldsymbol{\mu}_k)$
 - 8: **Fixed mesh solve:** Solve $\mathbf{r}(\mathbf{u}, \phi(\mathbf{y}_k^*); \boldsymbol{\mu}_k) = \mathbf{0}$ for \mathbf{u} with initial guess \mathbf{u}_k^* , replace $\mathbf{u}_k^* \leftarrow \mathbf{u}$
 - 9: **end for**
-

4.3. Application: Parameter continuation with early termination

Algorithm 1 is well-suited for many-query settings that require an accurate solution for every $\boldsymbol{\mu} \in \Xi$ such as parameter sweeps and “what-if” scenarios. However, applications such as optimization and continuation only need the solution at $\boldsymbol{\mu}_N$; solutions at all previous parameters either aid in finding $\boldsymbol{\mu}_N$ or robustly computing the solution at $\boldsymbol{\mu}_N$. As such, the solution at intermediate parameters $\boldsymbol{\mu}_1, \dots, \boldsymbol{\mu}_{N-1}$ can be computed approximately to improve computational efficiency. We focus on the continuation setting because the tolerances used for intermediate solutions in an optimization setting are intimately tied to global convergence theory [27] and beyond the scope of this work.

To this end, we introduce two convergence criteria based on (1) the number of iterations and (2) relative reduction of the DG residual. Let $(\mathbf{u}_k^i, \mathbf{y}_k^i)$ denote the i th iteration of the HOIST SQP solver at $\boldsymbol{\mu}_k$ with $(\mathbf{u}_k^0, \mathbf{y}_k^0) = (\mathbf{u}_{k-1}^*, \mathbf{y}_{k-1}^*)$. Then, we define the modified HOIST operator $\Upsilon_{n,\xi} : \mathbb{R}^{N_u} \times \mathbb{R}^{N_y} \times \mathcal{D} \rightarrow \mathbb{R}^{N_u} \times \mathbb{R}^{N_y}$ for $n > 1$ and $\xi < 1$ to be

$$\Upsilon_{n,\xi} : (\mathbf{u}_k^0, \mathbf{y}_k^0, \boldsymbol{\mu}_k) \mapsto (\tilde{\mathbf{u}}_k^*, \tilde{\mathbf{y}}_k^*) := (\mathbf{u}_k^I, \mathbf{y}_k^I), \quad (23)$$

where $I \leq n$ is the smallest number such that

$$\|\mathbf{r}(\mathbf{u}_k^I, \phi(\mathbf{y}_k^I); \boldsymbol{\mu}_k)\| \leq \xi \|\mathbf{r}(\mathbf{u}_k^0, \phi(\mathbf{y}_k^0); \boldsymbol{\mu}_k)\|. \quad (24)$$

That is, $(\tilde{\mathbf{u}}_k^*, \tilde{\mathbf{y}}_k^*)$ is the output of the HOIST SQP solver at parameter $\boldsymbol{\mu}_k$ after n iterations or when the residual converges to a relative tolerance of ξ , whichever occurs first. Then, we introduce iteration limits $n_1 \leq n_2$ and tolerances $\xi_2 \leq \xi_1$, and use Υ_{n_1, ξ_1} for intermediate parameters $k = 1, \dots, N-1$ and Υ_{n_2, ξ_2} for the last parameter $k = N$. The complete algorithm is summarized in Algorithm 2.

Algorithm 2 HOIST method for parameter continuation with parametrized lead shock

Input: Reference mesh of entire domain $\bar{\mathcal{E}}_h$, continuation set $\Xi = \{\boldsymbol{\mu}_1, \dots, \boldsymbol{\mu}_N\}$, tolerances (ξ_1, ξ_2) , iteration limits (n_1, n_2)

Output: HOIST solution at $\boldsymbol{\mu}_N$: $(\mathbf{u}_N^*, \mathbf{y}_N^*)$

- 1: **Initial HOIST solve:** Compute HOIST solution $(\tilde{\mathbf{u}}_1^*, \tilde{\mathbf{y}}_1^*)$ at $\boldsymbol{\mu}_1$ over $\bar{\mathcal{E}}_h$
 - 2: **Reduce mesh:** Create reduced mesh \mathcal{E}_h as $\bar{\mathcal{E}}_h$ without elements upstream of the lead shock
 - 3: **Transfer solution:** Transfer solution $\tilde{\mathbf{u}}_1^*$ to reduced mesh $\tilde{\mathbf{u}}_1^*$
 - 4: **Parametrize reduced mesh:** Determine parametrization of reduced mesh ϕ (Section 4.2)
 - 5: **Transfer mesh DoFs:** Transfer mesh DoFs $\tilde{\mathbf{y}}_1^*$ to reduced mesh $\tilde{\mathbf{y}}_1^*$
 - 6: **for** $k = 2, \dots, N - 1$ **do**
 - 7: **Approximate HOIST solve:** $(\tilde{\mathbf{u}}_k^*, \tilde{\mathbf{y}}_k^*) = \Upsilon_{n_1, \xi_1}(\tilde{\mathbf{u}}_{k-1}^*, \tilde{\mathbf{y}}_{k-1}^*, \boldsymbol{\mu}_k)$
 - 8: **end for**
 - 9: **Final parameter:** $(\mathbf{u}_N^*, \mathbf{y}_N^*) = \Upsilon_{n_2, \xi_2}(\tilde{\mathbf{u}}_{N-1}^*, \tilde{\mathbf{y}}_{N-1}^*, \boldsymbol{\mu}_N)$
 - 10: **Fixed mesh solve:** Solve $\mathbf{r}(\mathbf{u}, \phi(\mathbf{y}_N^*); \boldsymbol{\mu}_N) = \mathbf{0}$ for \mathbf{u} with initial guess \mathbf{u}_N^* , replace $\mathbf{u}_N^* \leftarrow \mathbf{u}$
-

5. Numerical experiments

In this section, we demonstrate the proposed HOIST framework for shock-dominated flow problems parametrized by the farfield Mach number (Section 5.1) and initial condition (Section 5.2). We examine the robustness of the framework under different solver settings to show the framework is able to accurately track the lead shock across parameter configurations and provide high-quality solutions on extremely coarse meshes.

5.1. Mach continuation

We begin by considering a series of compressible, inviscid flows with a bow shock that separates the boundary state from the downstream flow. We consider several simple bluff body flows (Section 5.1.1-5.1.3) that only possess a bow shock to study the method and close with flow over a double wedge geometry (Section 5.1.4) that has complex shock-shock interactions downstream of the bow shock. For these problems, the flow through the domain $\Omega \subset \mathbb{R}^d$ is modeled using the steady Euler equations

$$\begin{aligned}
 \frac{\partial}{\partial x_j} (\rho(x)v_j(x)) &= 0, \\
 \frac{\partial}{\partial x_j} (\rho(x)v_i(x)v_j(x) + P(x)\delta_{ij}) &= 0, \\
 \frac{\partial}{\partial x_j} ([\rho(x)E(x) + P(x)]v_j(x)) &= 0,
 \end{aligned} \tag{25}$$

for all $x \in \Omega$, where $i = 1, \dots, d$ and summation is implied over the repeated index $j = 1, \dots, d$. The density $\rho : \Omega \rightarrow \mathbb{R}_{>0}$, velocity $v_i : \Omega \rightarrow \mathbb{R}$ in the x_i direction for $i = 1, \dots, d$, and total energy $E : \Omega \rightarrow \mathbb{R}_{>0}$ of the fluid are implicitly defined as the solution of (25). We assume the fluid is an ideal gas that follows the thermal and caloric state equations

$$P = \rho RT, \quad e = \frac{1}{\gamma - 1} \frac{P}{\rho}, \tag{26}$$

where $P : \Omega \rightarrow \mathbb{R}_{>0}$ and $T : \Omega \rightarrow \mathbb{R}_{>0}$ are the pressure and temperature of the fluid, $e : \Omega \rightarrow \mathbb{R}_{>0}$ is the internal energy of the fluid, R is the specific gas constant, and γ is the ratio of specific heats. The frozen sound speed $c : \Omega \rightarrow \mathbb{R}_{>0}$ and Mach number $M : \Omega \rightarrow \mathbb{R}_{>0}$ are defined as

$$c^2 := \frac{\gamma P}{\rho}, \quad M := \frac{\sqrt{v_i v_i}}{c}. \tag{27}$$

From the definition of the specific total energy $E : \Omega \rightarrow \mathbb{R}_{>0}$ and total enthalpy $H : \Omega \rightarrow \mathbb{R}_{>0}$

$$E := e + \frac{v_i v_i}{2}, \quad H := \frac{\rho E + P}{\rho}, \quad (28)$$

the pressure of the fluid, $P : \Omega \rightarrow \mathbb{R}_{>0}$, is directly related to the conservative variables for an ideal gas as

$$P = (\gamma - 1) \left(\rho E - \frac{\rho v_i v_i}{2} \right). \quad (29)$$

The relationships between the downstream stagnation pressure p_{02} and the upstream pressure P_∞ , and between the stagnation temperature T_0 and the upstream temperature T_∞ , are defined through the upstream Mach number M_∞ and γ as

$$\frac{p_{02}}{P_\infty} = \frac{\left[\frac{(\gamma+1)M_\infty^2}{2} \right]^{\gamma/(\gamma-1)}}{\left[\left(\frac{2\gamma M_\infty^2}{\gamma+1} \right) - \left(\frac{\gamma-1}{\gamma+1} \right) \right]^{1/(\gamma-1)}}, \quad \frac{T_0}{T_\infty} = 1 + \frac{\gamma-1}{2} M_\infty^2. \quad (30)$$

Finally, the Euler equations can be written as a general system of conservation laws (1) as

$$U(x) = \begin{bmatrix} \rho(x) \\ \rho(x)v(x) \\ \rho(x)E(x) \end{bmatrix}, \quad F(U(x)) = \begin{bmatrix} \rho(x)v(x)^T \\ \rho v(x)v(x)^T + P(x)I \\ (\rho(x)E(x) + P(x))v(x)^T \end{bmatrix}, \quad S(U(x)) = 0.$$

Remark 2. *We found that it is necessary to use boundary conditions on the shock boundary that directly evaluate the physical flux at the boundary state, as opposed to boundary conditions based on Riemann solvers. We found that Riemann solver boundary conditions can fail to enforce the boundary state on the shock boundary and derail the implicit tracking process.*

5.1.1. Inviscid flow over cylinder, Mach continuation to $M_\infty = 3$

In this problem, we solve for steady $M_\infty = 3$ flow over a cylinder in $d = 2$ dimensions using Mach continuation beginning at $M_\infty = 2$. At $M_\infty = 3$, we have the following stagnation quantities, which will be used to make quantitative assessment of the accuracy of the HOIST method: $p_{02} = 12.061$, $T_0 = 2$, and $H_0 = 7$. Our approach begins by applying the HOIST method at $M_\infty = 2$ on a shock-agnostic mesh of the entire domain consisting of 229 elements and extracting the solution and mesh downstream of the lead shock to initialize our continuation strategy, resulting in a reduced mesh with 172 elements (Figure 1).

We examine the performance of the framework with different number of continuation stages, $N = 2, 5, 10, 20$. The intermediate stages are solved with at most $n_1 = 30$ iterations or to a tolerance of $\xi_1 = 10^{-4}$, and the final stage is solved with at most $n_2 = 100$ iterations or to a tolerance of $\xi_2 = 10^{-8}$. The HOIST solver parameters used for all Υ evaluations are $\lambda = 10^{-4}$, $\kappa_0 = 1$, and $(\zeta, \nu) = (4, 0.25)$ [23]. For all four cases, the SQP solver drives the DG residual $\|\mathbf{r}(\mathbf{u}_k^i, \phi(\mathbf{y}_k^i), \boldsymbol{\mu}_k)\|$ rapidly towards the early termination criteria for each intermediate stage; in the final stage, the enriched DG residual $\|\mathbf{R}(\mathbf{u}_N^i, \phi(\mathbf{y}_N^i), \boldsymbol{\mu}_N)\|$ plateaus within 15 iterations (Figure 2). Even though the DG residual does not reach a tight tolerance for any of the case, all cases exhibits deep convergence, i.e., $\|\mathbf{r}(\mathbf{u}, \phi(\mathbf{y}_N^I), \boldsymbol{\mu}_N)\| \sim \mathcal{O}(10^{-14})$, within 3 Newton iterations using the HOIST output as its starting point. Thus, the shock is indeed tracked and the fully discrete PDE is satisfied on the final discontinuity-aligned mesh, which shows the continuation framework is robust with as few as two stages.

The proposed framework produces well-resolved, accurate shock profiles and temperature and pressure distributions along the cylinder (Figure 3). The HOIST solver is robust in that it does not require parameter tuning across stages despite the changing Mach number. The value and the relative error of stagnation quantities evaluated at the stagnation point $(x_1, x_2) = (-1, 0)$ are reported in Table 1, which are all quite small, particularly considering the coarse grid used (only 172 quadratic elements). For the $N = 5$ case, Figure 4 shows the flow solution and mesh at all Mach numbers considered, including intermediate (partially converged) ones. In all cases, the shock is tracked with curved, high-order elements and the solution is well-resolved throughout the domain. The overall mesh quality is also well-preserved as the shock boundary

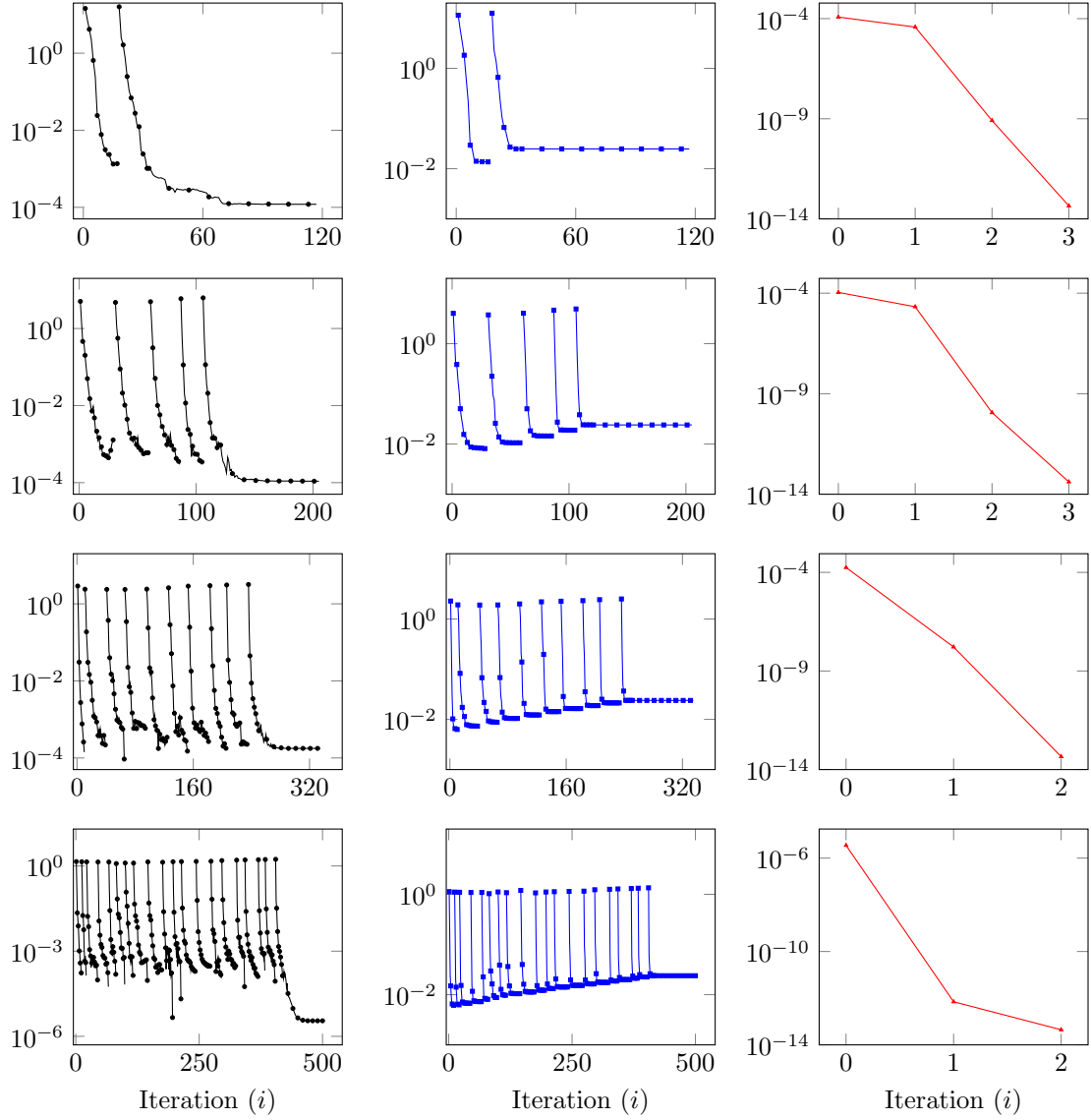


Figure 2: SQP convergence history of the DG residual $\|\mathbf{r}(\mathbf{u}_k^i, \phi(\mathbf{y}_k^i); \boldsymbol{\mu}_k)\|$ (\blackrightarrow) and enriched DG residual $\|\mathbf{R}(\mathbf{u}_k^i, \phi(\mathbf{y}_k^i); \boldsymbol{\mu}_k)\|$ (\bluearrow), and the DG residual throughout the fixed-mesh Newton iterations $\|\mathbf{r}(\mathbf{u}_i, \phi(\mathbf{y}_k^i); \boldsymbol{\mu}_k)\|$ (\redarrow) with $N = 2, 5, 10, 20$ (top to bottom) continuation stages for $M_\infty = 2$ to $M_\infty = 3$ continuation (cylinder).

is compressed towards the cylinder.

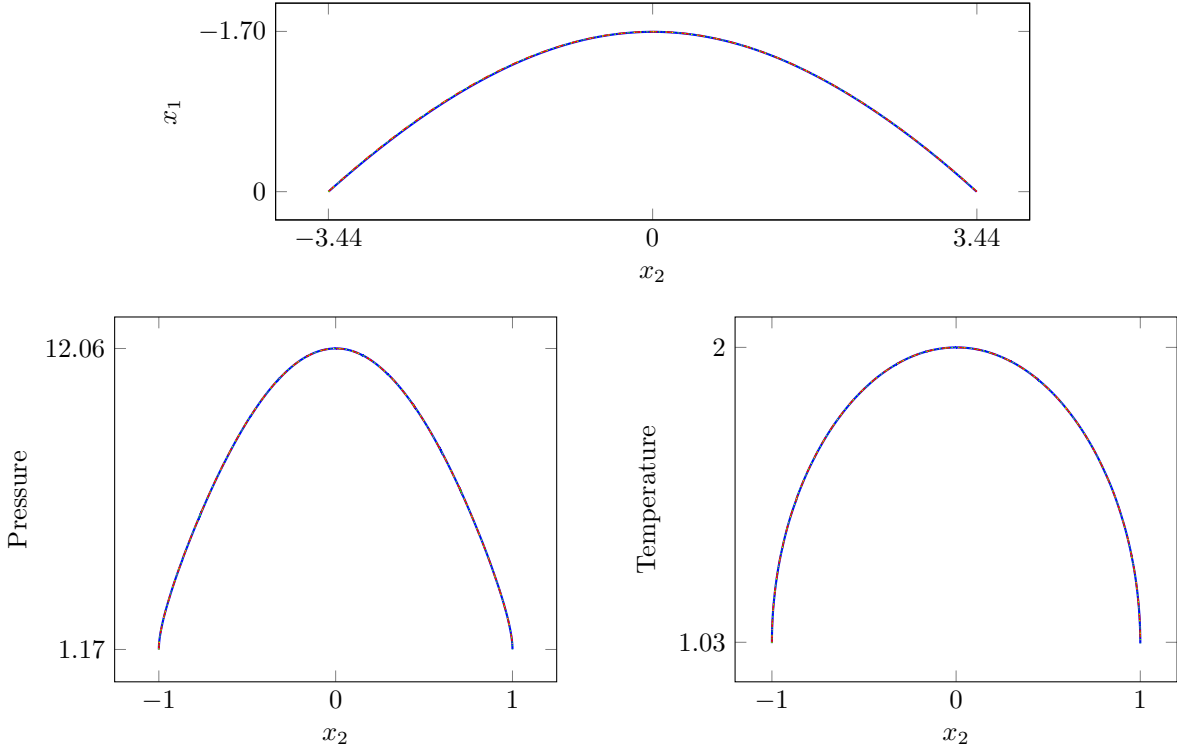


Figure 3: Lead shock position (*top*), and pressure (*bottom left*) and temperature (*bottom right*) along the surface of the cylinder at $M_\infty = 3$ using Mach continuation starting from $M_\infty = 2$ with $N = 2$ (—), $N = 5$ (---), $N = 10$ (⋯), and $N = 20$ (-·-·) stages.

5.1.2. Inviscid flow over cylinder, Mach continuation to $M_\infty = 10$

Next, we increase the difficulty of the previous problem by increasing the target Mach number to $M_\infty = 10$ using Mach continuation beginning at $M_\infty = 2$. In this case, the stagnation quantities are $p_{02} = 129.217$, $T_0 = 15$, and $H_0 = 52.5$. We use the same initial configuration as in Section 5.1.1 (after applying HOIST to the full domain at $M_\infty = 2$ and removing elements upstream of the bow shock), and we take the number of continuation stages to be $N = 40$ (5 stages per Mach number). The intermediate stages are solved with at most $n_1 = 30$ iterations or to a tolerance of $\xi_1 = 10^{-4}$, and the final stage is solved with at most $n_2 = 100$ iterations or to a tolerance of $\xi_2 = 10^{-8}$. We use the same HOIST solver parameters as in Section 5.1.1 and they remain the same throughout the optimization. In the final stage (from Mach 9.8 to Mach 10), the enriched DG residual $\|\mathbf{R}(\mathbf{u}_N^i, \phi(\mathbf{y}_N^i), \boldsymbol{\mu}_N)\|$ plateaus within 15 iterations (Figure 5) and the DG residual reaches a tolerance of 10^{-14} with only 4 fixed-mesh Newton iterations.

The proposed framework accurately tracks the shock and the fully discrete PDE is satisfied to a tight tolerance on the final discontinuity-aligned mesh. The framework robustly handled the large Mach variation that causes the shock to move significantly from its position at the initial Mach number $M_\infty = 2$ to the target Mach number $M_\infty = 10$ (Figures 3-7). The peak pressure and temperature along the surface are also significantly larger than the original $M_\infty = 2$ case, but are smooth and well-resolved nonetheless. The value and relative error of stagnation quantities evaluated at the stagnation point $(x_1, x_2) = (-1, 0)$ are reported in Table 1, which are still quite small. Figure 7 shows the flow solution and mesh at all Mach numbers considered, including intermediate (partially converged) ones. In all cases, the shock is tracked with curved, high-order elements and the solution is well-resolved throughout the domain. The overall mesh quality is also well-preserved as the shock boundary is substantially compresses toward the cylinder.

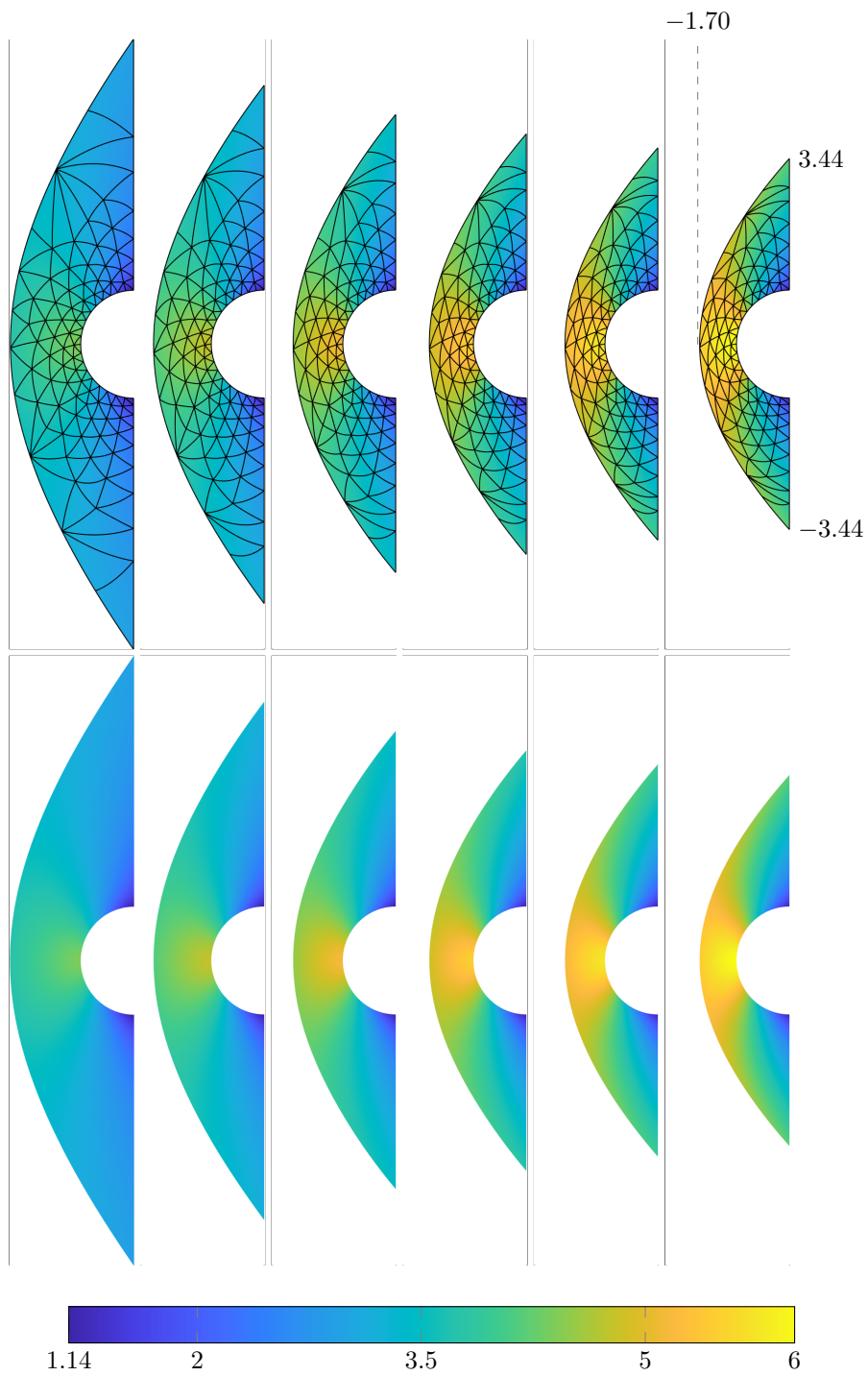


Figure 4: Density distribution at all continuation stages ($M_\infty = 2, 2.2, 2.4, 2.6, 2.8, 3$) for $N = 5$ (left to right).

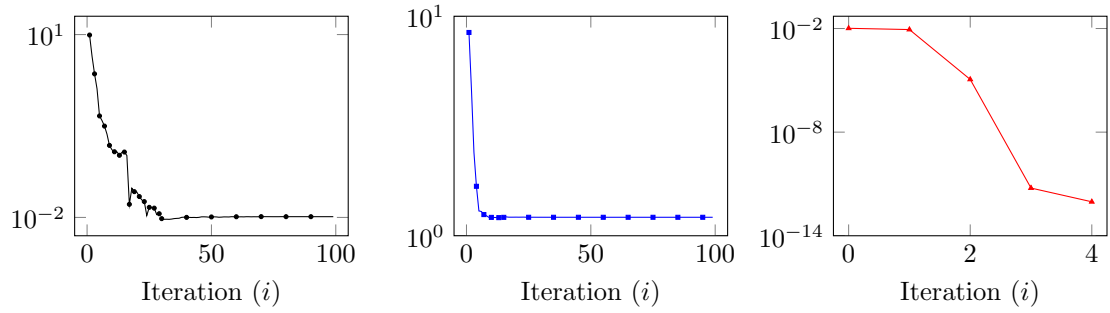


Figure 5: SQP convergence history of the DG residual $\|\mathbf{r}(\mathbf{u}_k^i, \phi(\mathbf{y}_k^i), \boldsymbol{\mu}_k)\|$ (\blackrightarrow), and the enriched DG residual $\|\mathbf{R}(\mathbf{u}_k^i, \phi(\mathbf{y}_k^i), \boldsymbol{\mu}_k)\|$ (\blackrightarrow), and the DG residual throughout the fixed-mesh Newton iterations $\|\mathbf{r}(\mathbf{u}_i, \phi(\mathbf{y}_k^i), \boldsymbol{\mu}_k)\|$ for the final stage from Mach 9.8 to 10 (\blackrightarrow) for $M_\infty = 2$ to $M_\infty = 10$ continuation (cylinder).

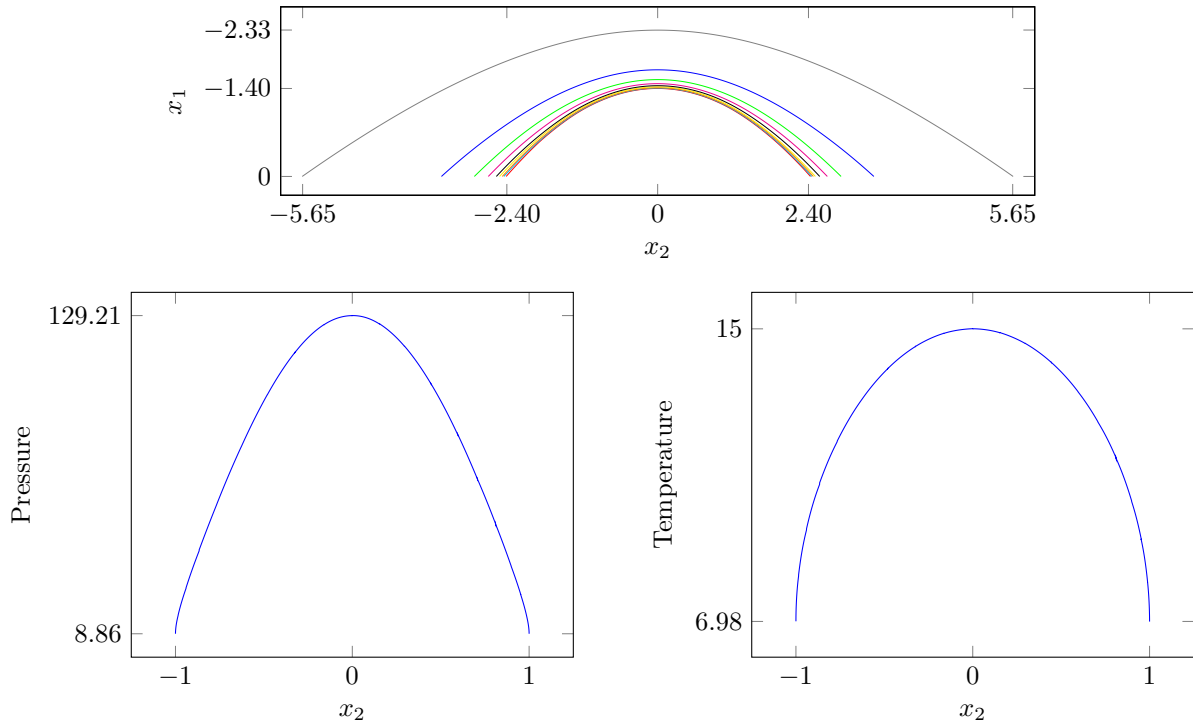


Figure 6: Lead shock positions (*top*) for $M_\infty = 2, 3, 4, \dots, 10$, and pressure (*bottom left*) and temperature (*bottom right*) along the surface of the cylinder at $M_\infty = 10$ using Mach continuation starting from $M_\infty = 2$ with $N = 40$ stages.

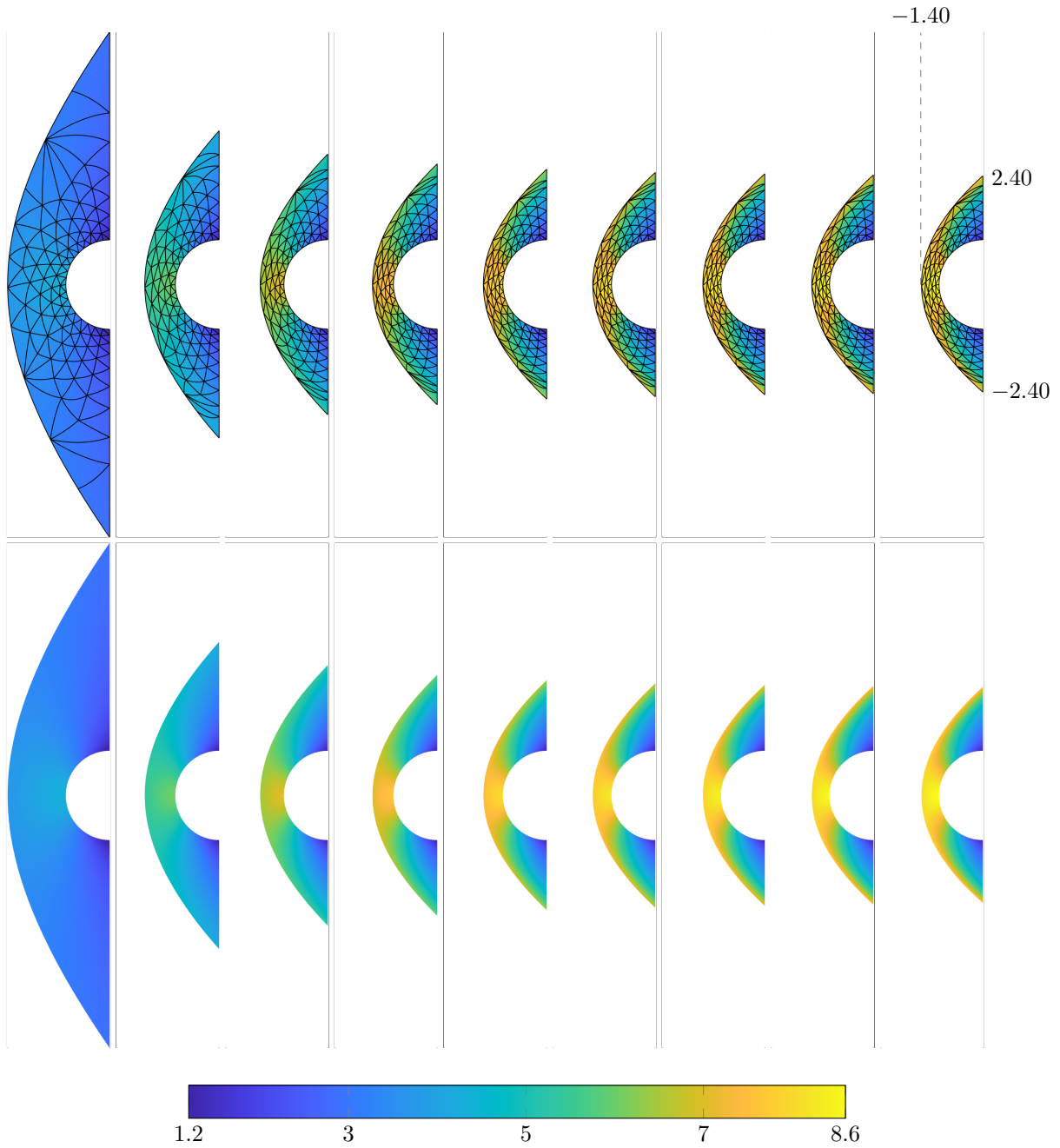


Figure 7: Density distribution at selected continuation stages ($M_\infty = 2, 3, 4, \dots, 10$) (left to right).

5.1.3. Inviscid flow over sphere, Mach continuation to $M_\infty = 3$

Next, we consider steady $M_\infty = 3$ flow over a sphere using Mach continuation beginning at $M_\infty = 2$. At $M_\infty = 3$, we have the following stagnation quantities, which will be used to make quantitative assessment of the accuracy of the HOIST method: $p_{02} = 12.061$, $T_0 = 2$, and $H_0 = 7$ (same as the 2D $M_\infty = 3$ case in Section 5.1.1). To reduce the computational cost, we model only an eighth of the geometry and use symmetry boundary conditions. Our approach begins by applying the HOIST method at $M_\infty = 2$ on a shock-agnostic mesh of the entire domain consisting of 491 elements and extracting the solution and mesh downstream of the bow shock to initialize our continuation strategy, resulting in a reduced mesh with 159 elements (Figure 8).

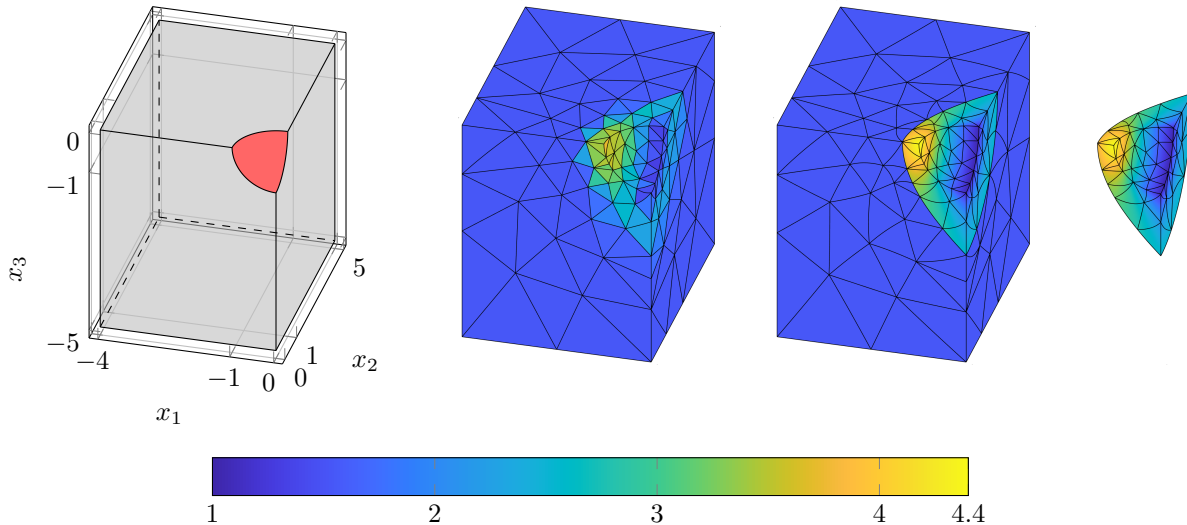


Figure 8: Flow domain (*left*) and the $M_\infty = 2$ initial guess (density) on a shock-agnostic mesh (*middle-left*), the shock-aligned mesh and corresponding solution obtained using HOIST (*middle-right*), and the corresponding solution and mesh extracted from downstream the bow shock (*right*).

We apply our continuation strategy with $N = 10$ stages. The intermediate stages are solved with at most $n_1 = 15$ iterations or to a tolerance of $\xi_1 = 10^{-4}$, and the final stage is solved with at most $n_2 = 100$ iterations or to a tolerance of $\xi_2 = 10^{-8}$. We use the same HOIST solver parameters as in Section 5.1.1 for all intermediate stages, and we set $\lambda = 0.5$, $\kappa_0 = 10^{-12}$ in the final stage to allow the solver to further improve the solution. Similarly rapid convergence of the HOIST solver and fixed-mesh solve in the final stage as the two-dimensional problems are observed (Figure 9). Figure 10 shows the flow solution and mesh at the initial ($M_\infty = 2$) and final ($M_\infty = 3$) Mach numbers. We observe that the high-order elements conform to the curvature of the bow shock, which leads to a highly accurate solution on an extremely coarse mesh (only 159 quadratic elements) when combined with the high-order flow field approximation. The overall mesh quality is well-preserved as the shock boundary and mesh elements compress towards the sphere. The value and relative error of stagnation quantities evaluated at the stagnation point $(x_1, x_2, x_3) = (-1, 0, 0)$ are reported in Table 1, which demonstrates the high accuracy per DoF of the overall approach for three-dimensional problems.

5.1.4. Inviscid flow over double wedge, Mach continuation to $M_\infty = 6.8$

Next, we consider steady $M_\infty = 6.8$ flow over a double-wedge geometry with angles 15° and 35° using Mach continuation beginning at $M_\infty = 2.8$. Our approach begins by applying the HOIST method at $M_\infty = 2.8$ on a shock-agnostic mesh of the entire domain consisting of 681 elements and extracting the solution and mesh downstream of the lead shock to initialize our continuation strategy, resulting in a reduced mesh with 576 elements (Figure 11). In this experiment, the shock boundary consists of an oblique shock followed by a bow shock, which introduces highly non-uniform mesh motion during the parameter sweep. In addition, this problem possesses complex shock-shock interactions and a supersonic jet downstream of the lead shock as M_∞ is increased.

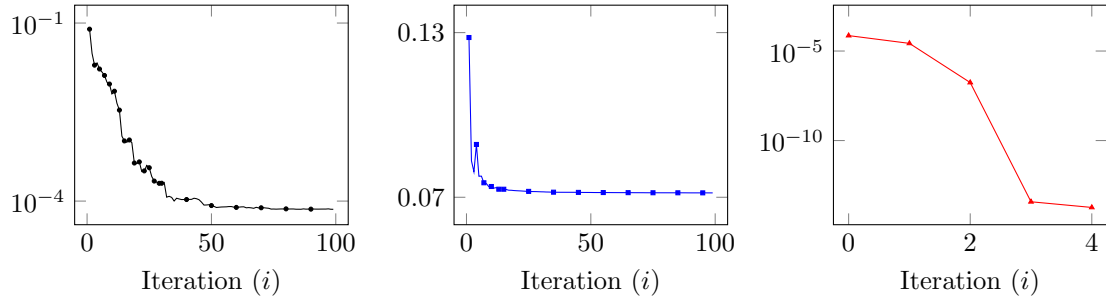


Figure 9: SQP convergence history of the DG residual $\|\mathbf{r}(\mathbf{u}_k^i, \phi(\mathbf{y}_k^i), \boldsymbol{\mu}_k)\|$ (\blackrightarrow) and enriched DG residual $\|\mathbf{R}(\mathbf{u}_k^i, \phi(\mathbf{y}_k^i), \boldsymbol{\mu}_k)\|$ (\bluearrow), and the DG residual throughout the fixed-mesh Newton iterations $\|\mathbf{r}(\mathbf{u}_i, \phi(\mathbf{y}_k^i), \boldsymbol{\mu}_k)\|$ for the final stage from Mach 2.9 to 3 (\redarrow) for $M_\infty = 2$ to $M_\infty = 3$ continuation (sphere).

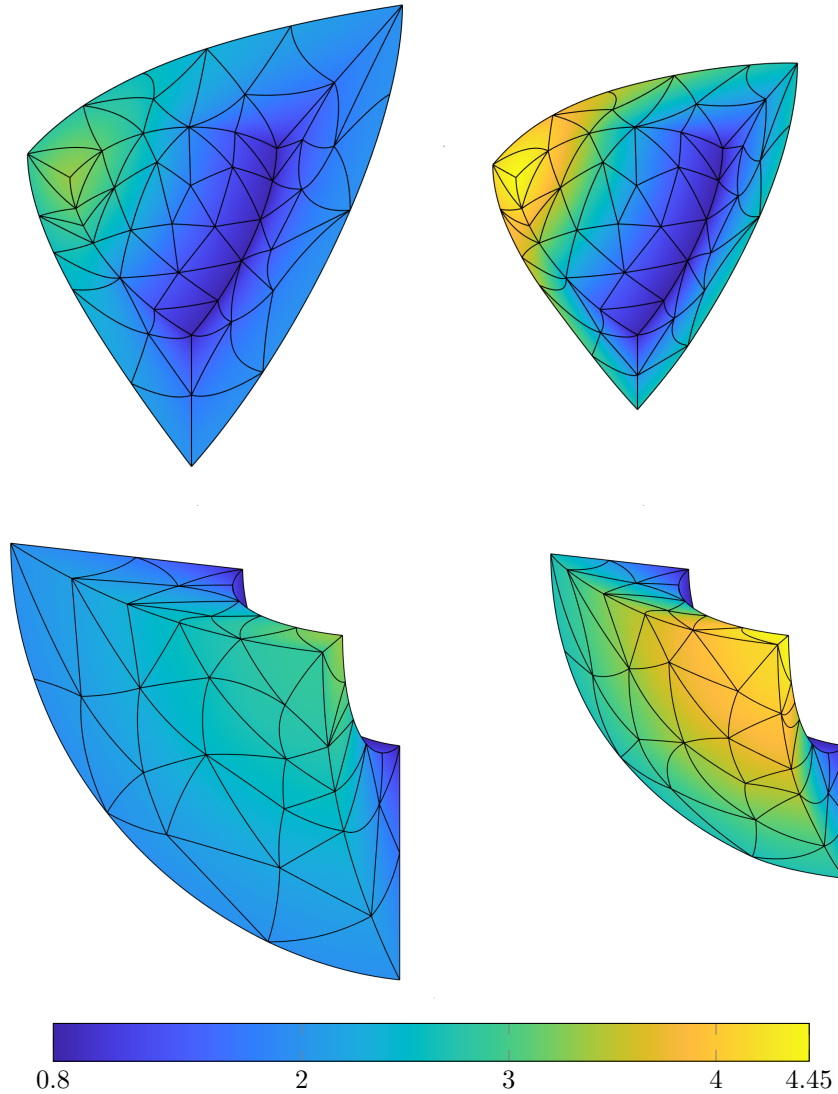


Figure 10: Density distribution at the initial $M_\infty = 2$ (left) and final $M_\infty = 3$ (right) continuation stage with two views (top to bottom).

Table 1: Quantities of interest at the stagnation point produced by HOIST method at final continuation stage (\check{p}_{02} , \check{T}_0 , \check{H}_0) and the corresponding relative error for all numerical experiments.

	N	\check{p}_{02}	$ p_{02} - \check{p}_{02} /p_{02}$	\check{T}_0	$ T_0 - \check{T}_0 /T_0$	\check{H}_0	$ H_0 - \check{H}_0 /H_0$
$M = 3, 2D$	2	12.0610	6.8939e-06	1.9999	5.9976e-05	6.9996	5.8529e-05
	5	12.0588	1.7742e-04	1.9998	9.4091e-05	6.9994	9.2435e-05
	10	12.0592	1.4654e-04	1.9999	5.3712e-05	6.9996	5.1601e-05
	20	12.0587	1.9162e-04	1.9998	8.3470e-05	6.9994	8.1685e-05
$M = 10, 2D$	40	129.2054	8.9226e-05	15.0029	1.9480e-04	52.5104	1.9905e-04
$M = 3, 3D$	10	11.9799	6.7254e-03	1.9990	5.1980e-04	6.9966	4.8529e-04

We apply our continuation strategy with $N = 121$ stages. The intermediate stages are solved with $n_1 = 50$ iterations and the final stage is solved with $n_2 = 100$ iterations. The HOIST solver parameters used for all Υ evaluations are $\lambda = 10^{-1}$, $\kappa_0 = 10^{-2}$, and $(\zeta, \nu) = (2, 0.5)$ [23]. Figure 12 shows the flow solution and mesh at selected Mach numbers during the parameter sweep. The density range varies drastically from the initial Mach 2.8 flow to the final Mach 6.8 flow, and complex shock-shock interactions emerge. As the inflow Mach increases, a Type IV shock interaction [32] is observed and a thin layer of elements conforms to the curved supersonic jet.

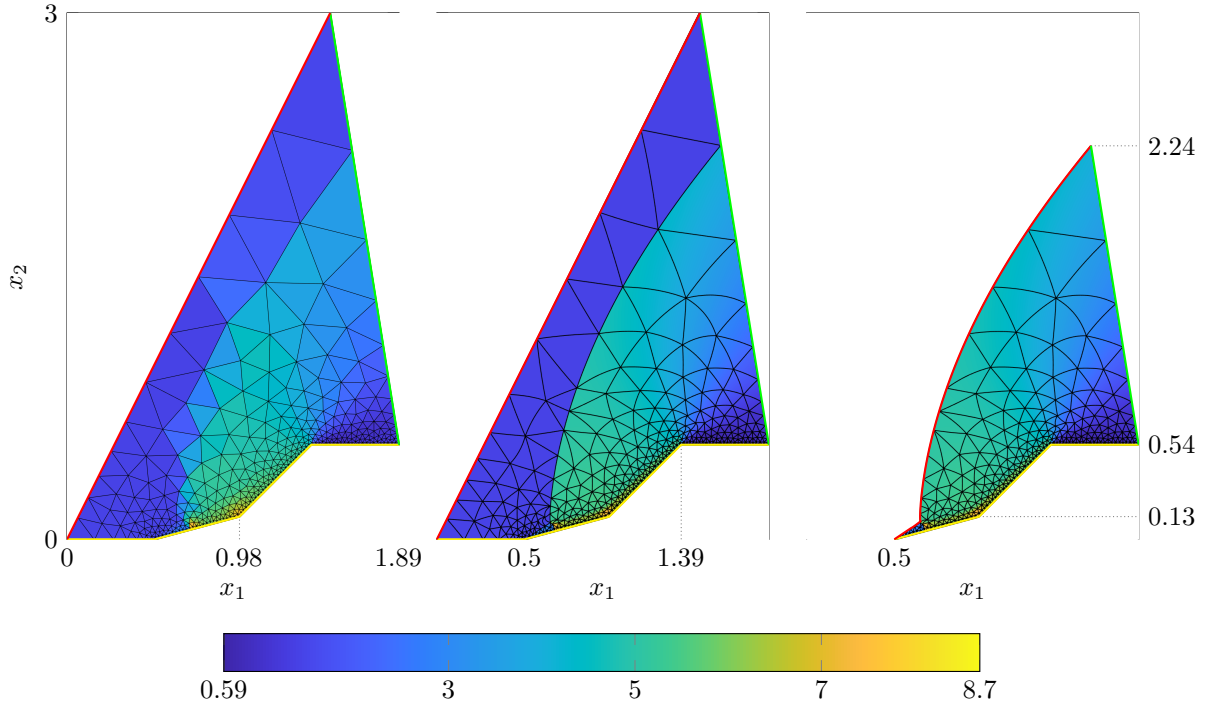


Figure 11: Initial guess (density) on a shock-agnostic mesh of $M_\infty = 2.8$ flow over the double-wedge geometry (*left*), the shock-aligned mesh and corresponding solution obtained using HOIST (*middle*), and the corresponding solution and mesh extracted from downstream the lead shock (*right*). The corresponding boundary conditions are inflow (—), slip walls (—), and outflow (—).

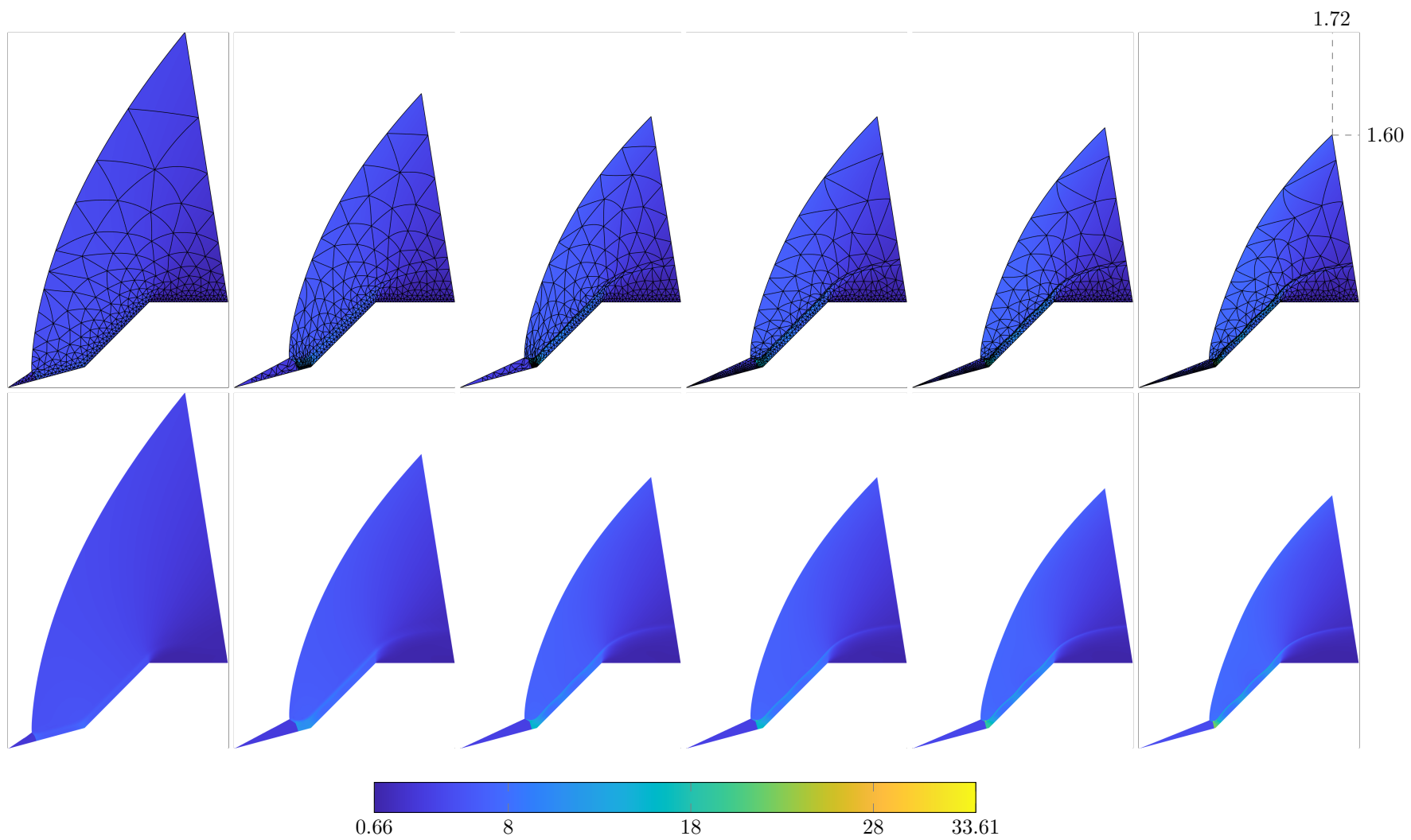


Figure 12: Density distribution for double-wedge simulation (left to right): $M_\infty = 2.8$, $M_\infty = 3.77$, $M_\infty = 4.77$ (stage 60, before re-mesh), $M_\infty = 4.77$ (stage 60, after re-mesh), $M_\infty = 5.77$, and $M_\infty = 6.8$.

Due to the nature of this problem, the elements condense near the intersection of the two wedges at $(x_1, x_2) = (0.98, 0.13)$ forming long and skinny triangles as the Mach number increases. These unavoidably crowded elements can degrade the solution quality, which necessitates re-meshing at an intermediate parameter stage. We choose to re-mesh at the middle of the parameter sweep without any attempt to preserve internal shock structures or even the shock boundary. After the re-mesh, we use the HOIST method with a free shock boundary to re-solve the stage to recover the appropriate lead shock position and internal shock structure. As shown in Figure 13, the initial re-meshed configuration of 837 elements is shock-agnostic with respect to the shock interactions downstream the lead shock, and the tracked configuration of 809 elements resolves those solution features.

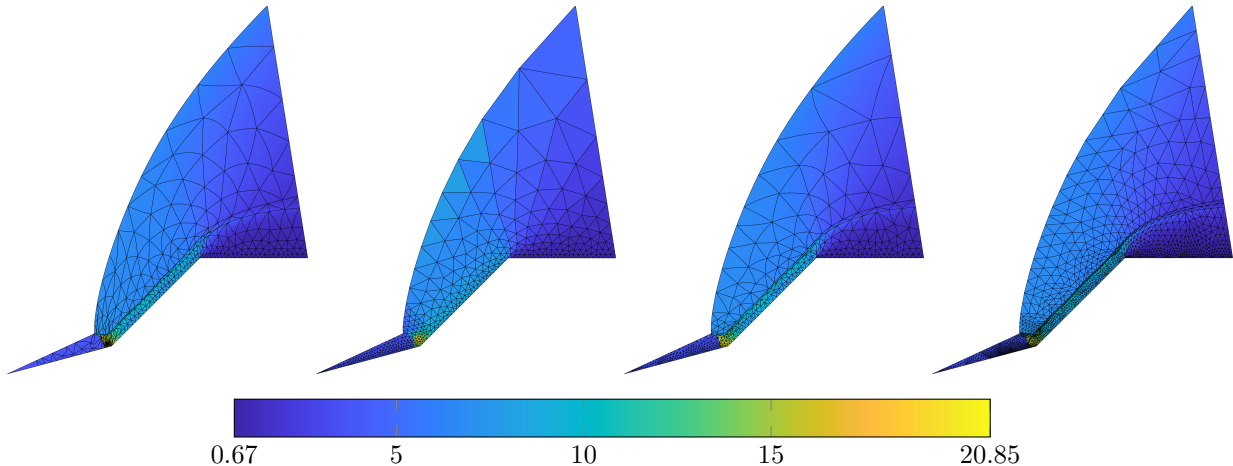


Figure 13: Density distributions at $M_\infty = 4.77$ (stage 60) for double-wedge simulation: before re-mesh (*left*), after re-mesh with a piecewise constant initial guess for the flow solution (*middle-left*), the HOIST solution after re-mesh (*middle-right*), and the HOIST solution after refinement of new mesh (*right*).

Despite the lead shock being accurately tracked, we observe the complex shock interactions have a low resolution and the contact discontinuity is not well-tracked on the coarse mesh as shown in Figure 14. This is due to the low mesh element density in the shock interaction region. As such, we refine the mesh at stage 60 (immediately after the re-mesh and solve), which leads to a grid with 2846 elements, and use the HOIST method to compute the corresponding refined solution (Figure 13). From this mesh and solution, the Mach continuation strategy continues until $M_\infty = 6.8$ is reached with $n_1 = 30$. While the lead shock and solution are visually indistinguishable, a close look at the shock interaction region shows the refined mesh tracks and resolves the Type IV interaction and contact much better. Furthermore, the refined mesh compresses more elements into the supersonic jet to better resolve it. Finally, we show the positions of the lead shock at selected parameter stages (Figure 15) and note the re-mesh at stage 60 did not disrupt the lead shock location because the shock positions overlap (1) before and after the re-mesh at stage 60 and (2) on the coarse and fine mesh at $M_\infty = 6.8$.

To close this study, we justify the reduced-mesh Mach continuation approach relative to directly applying the HOIST method to the parameter of interest. For this, we return to the full domain and use HOIST to directly solve the problem at $M_\infty = 5.8$ (stage 91). In this setting, we observe poorly conditioned elements upstream of the lead shock, numerous element collapses near the beginning of the first wedge, an inaccurate lead shock position, and under-resolved shock interactions. These issues can be avoided by either using a refined mesh or the proposed continuation approach (Figure 12).

5.2. Initial condition sweep

To demonstrate the flexibility of the proposed many-query framework beyond Mach continuation, we close by considering a parametrized Riemann problem of the Euler equations. The Euler equations model

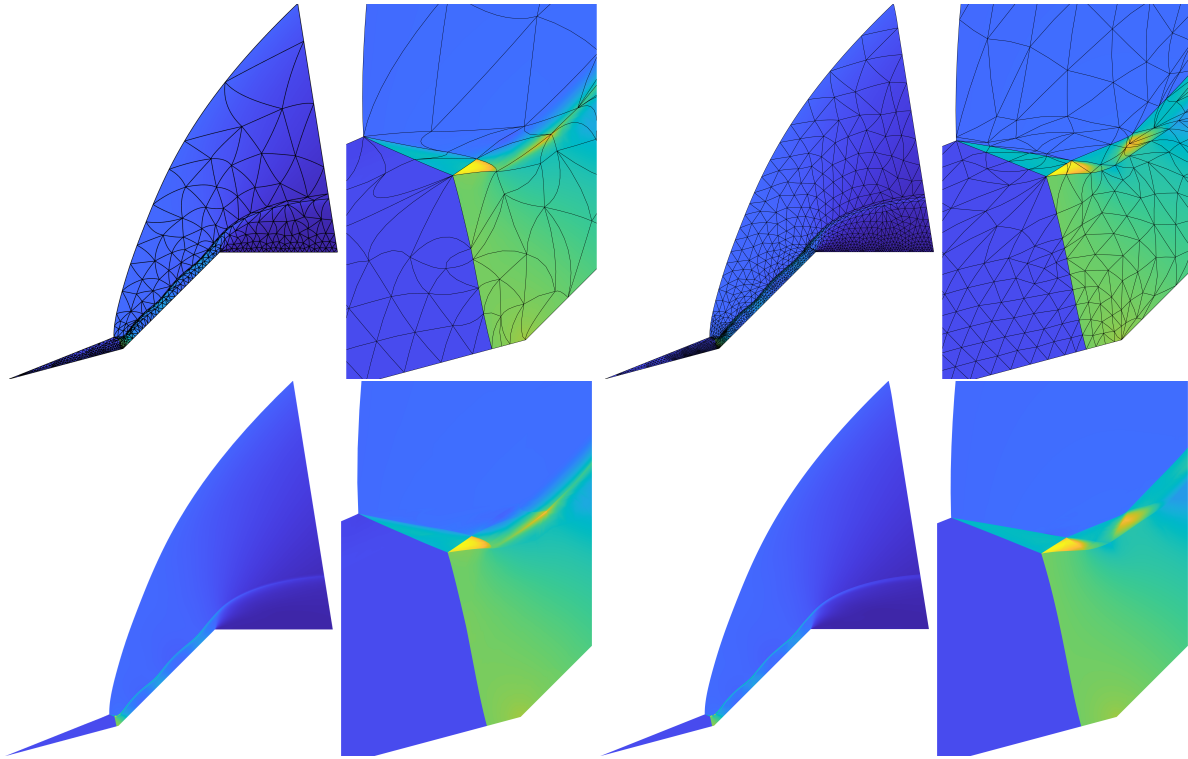


Figure 14: Density distribution at $M_\infty = 6.8$ for double-wedge simulation: coarse mesh (*left*), coarse mesh with shock interaction blown up (*middle-left*), refined mesh (*right-middle*), and refined mesh with shock interaction blown up (*right*). Colorbar in Figure 12.

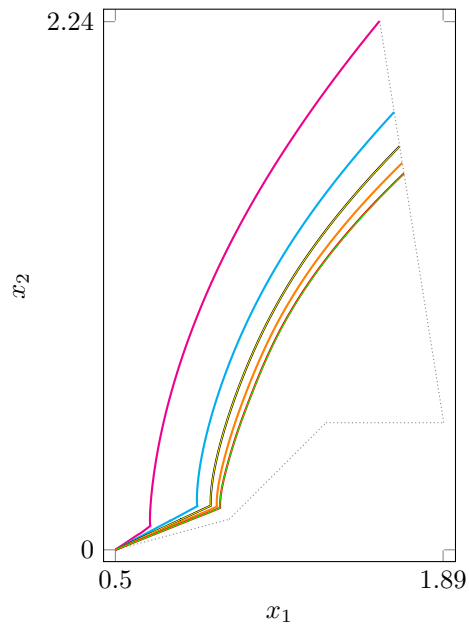


Figure 15: Lead shock positions for the double wedge simulation: $M_\infty = 2.8$ (—), $M_\infty = 3.77$ (—), $M_\infty = 4.77$ (stage 60 before re-mesh) (—), $M_\infty = 4.77$ (stage 60 after re-mesh) (—), $M_\infty = 5.77$ (—), $M_\infty = 6.8$ (final stage, coarse mesh) (—), $M_\infty = 6.8$ (final stage, fine mesh) (—).

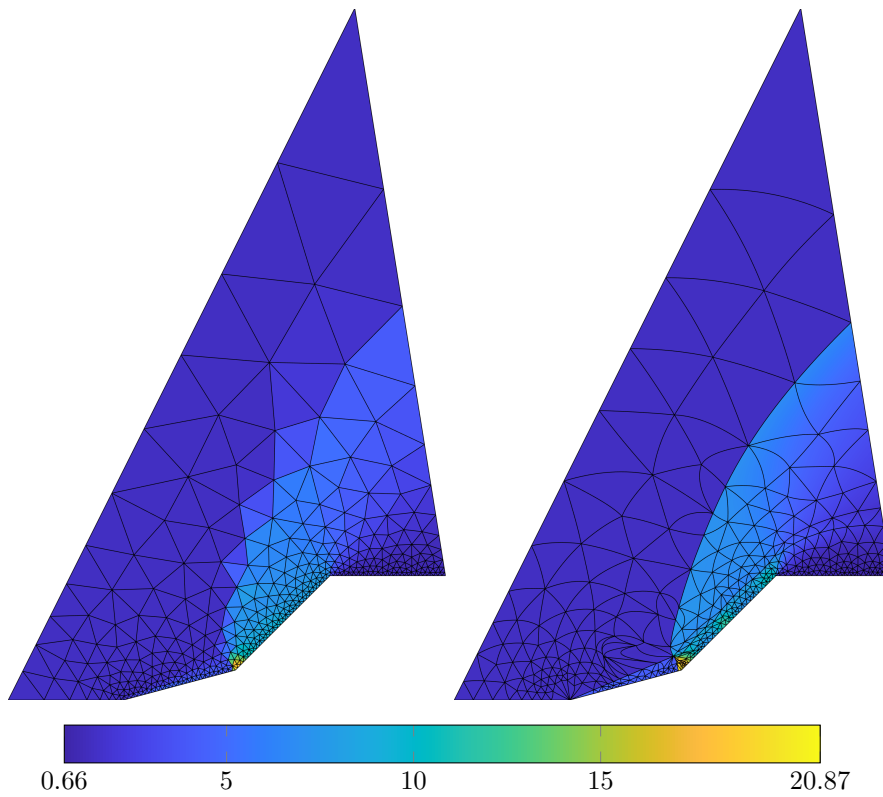


Figure 16: Initial guess (density) on a shock-agnostic mesh (full domain) of $M_\infty = 5.8$ flow over the double-wedge geometry (*left*) and the HOIST solution (*right*). Mesh motion from the shock-upstream portion of the domain introduces poorly conditioned elements.

unsteady, compressible flow in a one-dimensional domain $\Omega \subset \mathbb{R}$ and read

$$\begin{aligned} \frac{\partial}{\partial t} \rho(x, t) + \frac{\partial}{\partial x} (\rho(x, t)v(x, t)) &= 0, \\ \frac{\partial}{\partial t} (\rho(x, t)v(x, t)) + \frac{\partial}{\partial x} (\rho(x, t)v(x, t)^2 + P(x, t)) &= 0, \\ \frac{\partial}{\partial t} (\rho(x, t)E(x, t)) + \frac{\partial}{\partial x} ([\rho(x, t)E(x, t) + P(x, t)]v(x, t)) &= 0, \end{aligned} \quad (31)$$

for all $x \in \Omega$ and $t \in \mathcal{T}$, where $\mathcal{T} := (0, T]$ is the temporal domain and $T \in \mathbb{R}_{>0}$ is the final time. The density $\rho : \Omega \times \mathcal{T} \rightarrow \mathbb{R}_{>0}$, velocity $v : \Omega \times \mathcal{T} \rightarrow \mathbb{R}$, and total energy $E : \Omega \times \mathcal{T} \rightarrow \mathbb{R}_{>0}$ of the fluid are implicitly defined as the solution of (31). We assume the fluid is an ideal gas, which leads to the relationship between pressure and energy in (29). Finally, the Euler equations can be written as a general system of steady conservation laws (1) over the space-time domain $\Omega \times \mathcal{T}$ with space-time coordinate $z = (x, t)$ as

$$U(z) = \begin{bmatrix} \rho(x, t) \\ \rho(x, t)v(x, t) \\ \rho(x, t)E(x, t) \end{bmatrix}, \quad F(U(z)) = \begin{bmatrix} \rho(x, t)v(x, t) & \rho(x, t) \\ \rho(x, t)v(x, t)^2 + P(x, t) & \rho(x, t)v(x, t) \\ (\rho(x, t)E(x, t) + P(x, t))v(x, t) & \rho(x, t)E(x, t) \end{bmatrix}, \quad S(U(z)) = 0.$$

We consider a Riemann problem of the Euler equations (31) with the following parametrized initial condition

$$(\rho(x, 0), v(x, 0), P(x, 0)) = \begin{cases} (\rho_L, 0, P_L(\mu)) & x < 0.5 \\ (\rho_R(\mu), 0, P_R(\mu)) & x \geq 0.5, \end{cases} \quad (32)$$

where $\mu \in \mathcal{D} := [0, 1]$ and

$$P_L(\mu) = 25\mu + (1 - \mu), \quad \rho_R(\mu) = 0.35\mu + 0.125(1 - \mu), \quad P_R(\mu) = 0.075\mu + 0.1(1 - \mu) \quad (33)$$

over the spatial domain $\Omega := (0, 1)$ and temporal domain $\mathcal{T} = (0, 0.2]$. At $\mu = 0$, this corresponds to the canonical Sod shock tube and possesses similar features to the Woodward-Colella blast [38] at $\mu = 1$. The discontinuity magnitudes and propagation speed of the waves varies significantly for $\mu \in \mathcal{D}$. Because larger values of μ will have faster waves, we allow the final time to vary with μ such that the waves travel approximately the same distance in \mathcal{T} . That is, we let $T = T(\mu)$ with $T(0) = 0.2$ and final time for other parameters determined using the HOIST framework.

Following the proposed procedure, we begin with a shock-agnostic mesh of the space-time domain consisting of 82 triangles and apply the HOIST method at $\mu = 0$ (Sod) to create a shock-aligned mesh and the corresponding solution. We use linear ($q = 1$) mesh elements and quadratic ($p = 2$) solution approximation because all non-smooth features are straight-sided for any $\mu \in \mathcal{D}$ and the solution inside the rarefaction is nonlinear. At $\mu = 0$, the solution possesses a shock wave, contact discontinuity, and rarefaction wave, with both the shock wave and head of the rarefaction qualifying as lead ‘‘shocks’’ (non-smooth features separating a boundary from the remainder of the flow). Finally, we remove all elements left of the rarefaction and right of the shock wave, except one layer of upstream elements are retained (not shown in figure for clarity) to improve boundary condition enforcement, to create a reduced mesh of 42 elements (Figure 17).

From this configuration, we perform a parameter sweep to reliably compute the HOIST solution at $N = 125$ uniformly spaced samples in \mathcal{D} (Figure 18). The HOIST solver parameters used for all Υ evaluations are $\lambda = 10^{-1}$, $\kappa_0 = 10^{-6}$, and $(\zeta, \nu) = (2, 0.5)$. To handle the parameter-dependent final time $T(\mu)$, we allow the HOIST solver to determine the location of the top boundary ($t = T$). Figure 18 shows four selected parameter configurations. The upper temporal boundary adjusts to ensure the waves travel roughly the same spatial distance. At $\mu = 0$, the speed of the shock is approximately 1.75 and the density jump magnitude is about 2, whereas at $\mu = 1$, the shock speed is 5.3 and the density jump is 5.7. Finally, it can be seen that for larger values of μ , the speed of the shock and contact are close, which makes the constant wedge between the shock and contact slender with a sharp angle. We have observed that thin regions like this can be difficult to directly track from a shock-agnostic mesh, often requiring a much finer mesh so elements can fit to the region without being collapsed. The proposed many-query setting alleviates this burden by initializing these difficult situations from nearly aligned grids (from a HOIST solve at a different parameter configuration).

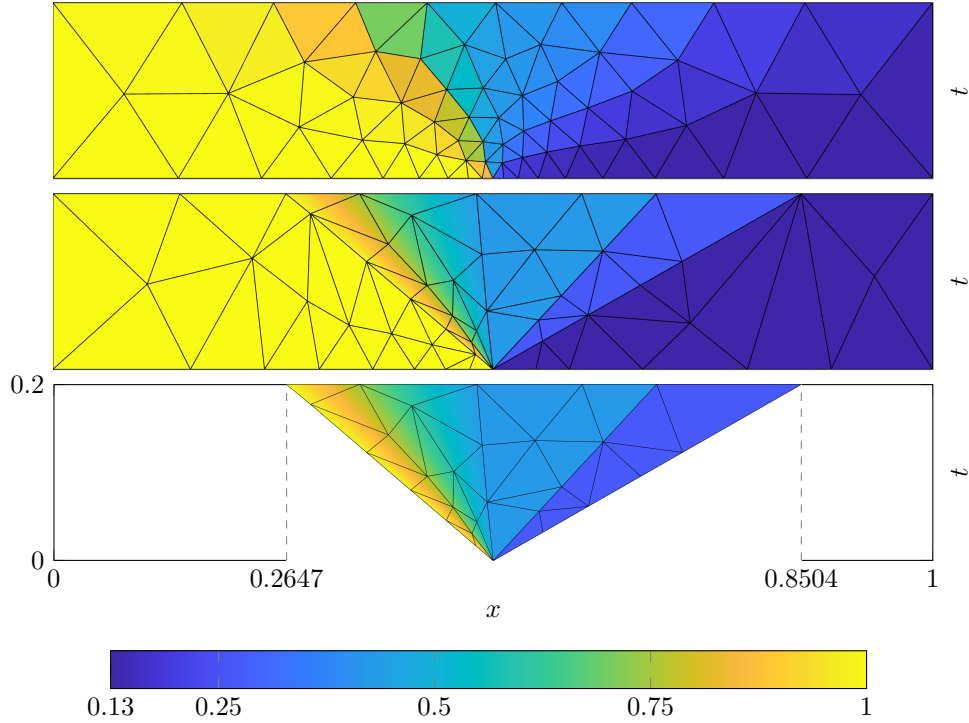


Figure 17: Initial guess (density) on a shock-agnostic space-time mesh for the Riemann problem at $\mu = 0$ (*top*), the shock-aligned mesh and corresponding solution obtained using HOIST (*middle*), and the corresponding solution and mesh extracted from the region to the left of the rarefaction head and right of the shock (*bottom*).

Finally, we verify the HOIST solution at the extremal parameters ($\mu = 0, 1$). At $\mu = 0$ (Sod) we compare to the exact solution at the final time $T(\mu = 0)$ and at $\mu = 1$ we compare to a highly refined second-order finite volume simulation at the final time $T(\mu = 1) = 0.039$. At both parameters, the HOIST solution matches the reference solution well with the shock, contact, and head and tail of the rarefaction tracked (Figure 19). This also shows the dramatic variation the solution undergoes as the parameter varies throughout \mathcal{D} .

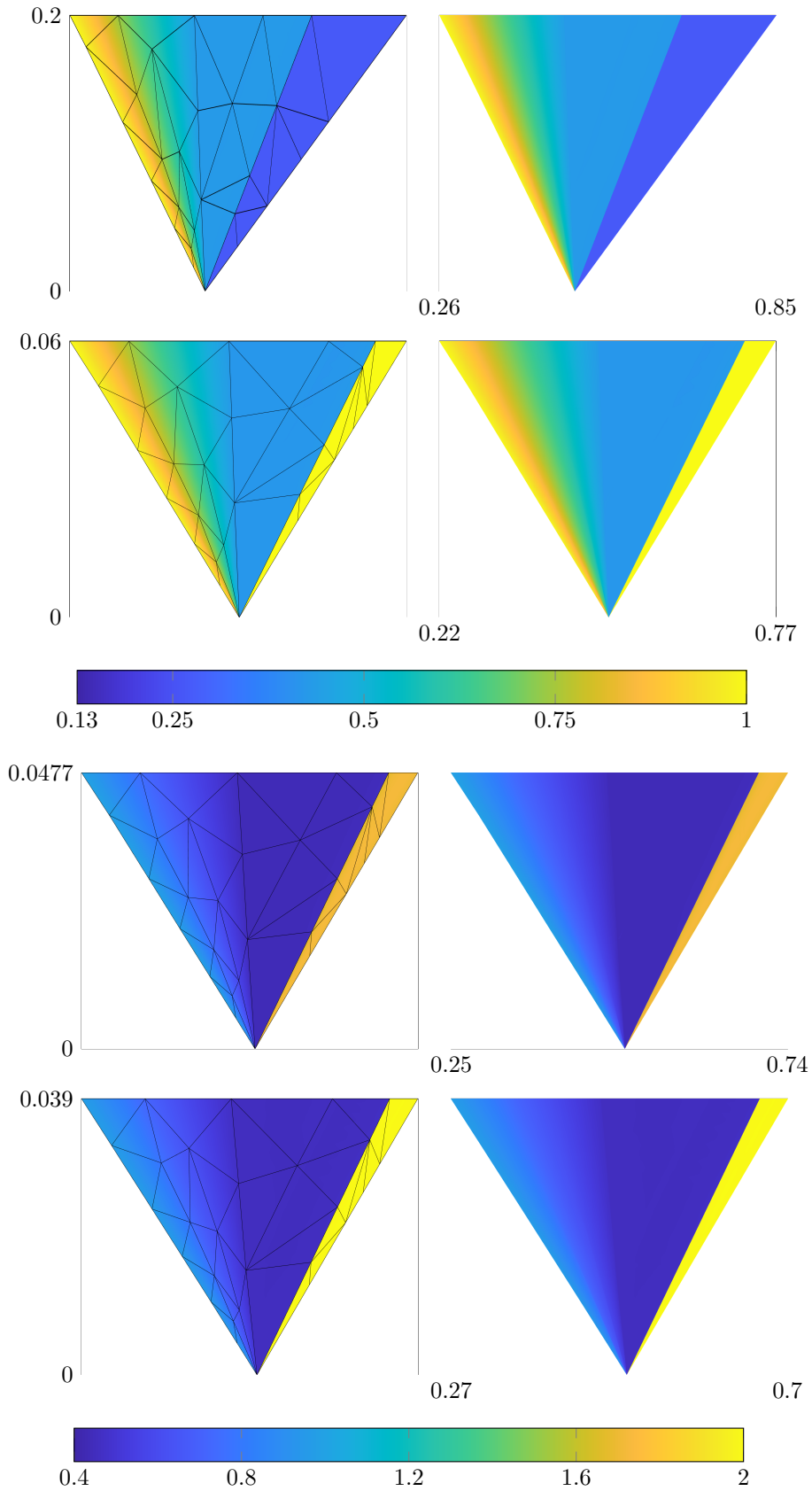


Figure 18: Space-time density distribution at $\mu = 0, 0.6, 0.8, 1.0$ (top to bottom).

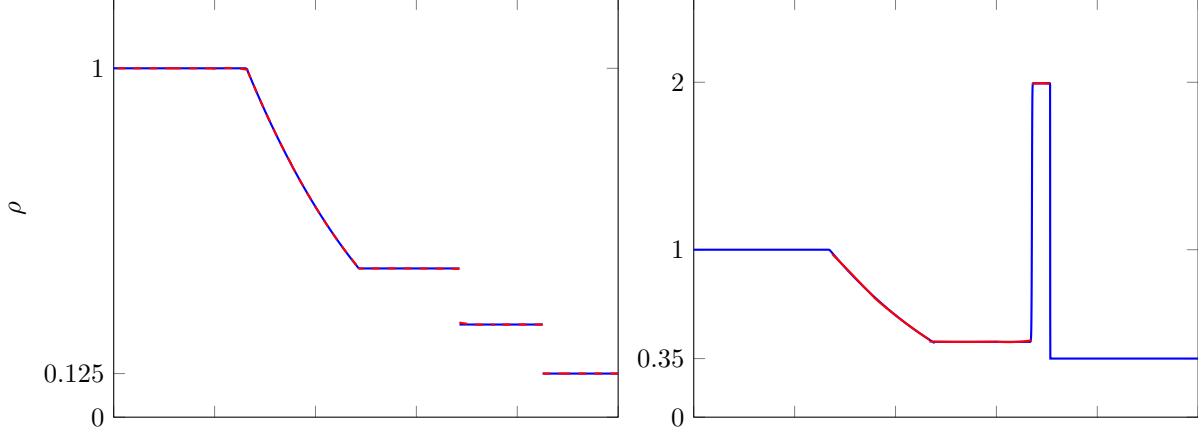


Figure 19: Density slices at final time for $\mu = 0$ (left) and $\mu = 1$ (right) for the HOIST solution (---) and reference solution (—).

6. Conclusion

We introduce a specialized version of the high-order implicit shock tracking framework, originally developed in [42, 23], for problems with parametrized lead shocks. The approach applies implicit shock tracking (e.g., HOIST [42, 23] or MDG-ICE [14]) on a shock-agnostic mesh at one parameter configuration of interest to generate a shock-aligned mesh and the corresponding flow field. All elements upstream of the lead shock are removed to produce a reduced mesh that will be used for all subsequent parameter configurations, with the farfield boundary condition directly applied on the shock boundary. In addition to the significant reduction in elements (up to a factor of three in this work), further reduction in the mesh DoFs is possible when the lead shock is the only non-smooth feature in the domain because only nodes on the shock boundary are optimized; the remainder are determined from boundary constraints and PDE-based smoothing. As a result, the shock boundary deforms as the parameters change and the remaining nodes are positioned to improve element quality. In addition to reducing the overall degrees of freedom of the implicit shock tracking discretization, this also improves robustness and accelerates convergence because the overall shock-fitting problem is easier and a high-quality initial guess is provided from the solution at previous parameter configurations. The proposed framework can be used for most *many-query* applications involving parametrized lead shocks such as optimization, uncertainty quantification, parameter sweeps, “what-if” scenarios, or parameter-based continuation.

In this work, we use the abstract many-query setting for Mach number continuation in steady inviscid flows and initial condition sweep for one-dimensional Riemann problems. For continuation, we leverage partially converged solves at intermediate stages to improve the efficiency of the approach. A set of numerical experiments, which include two- and three-dimensional supersonic and hypersonic flows, demonstrate the robustness and flexibility of the proposed framework, in particular, the same HOIST solver parameters can be used throughout the continuation process despite substantial variations in Mach number (from $M_\infty = 2$ to $M_\infty = 10$) and initial state. The framework was also shown to facilitate shock tracking for complex flow features downstream of the lead shock, as demonstrated by the flow over the double wedge where the shock interactions and supersonic jet were tracked and well-resolved by the approach.

Acknowledgments

This work is supported by AFOSR award numbers FA9550-20-1-0236, FA9550-22-1-0002, FA9550-22-1-0004, and ONR award number N00014-22-1-2299. The content of this publication does not necessarily reflect the position or policy of any of these supporters, and no official endorsement should be inferred.

References

- [1] Alessia Assonitis, Renato Paciorri, and Aldo Bonfiglioli. Numerical simulation of shock/boundary-layer interaction using an unstructured shock-fitting technique. *Computers & Fluids*, 228:105058, 2021.
- [2] Garrett E. Barter and David L. Darmofal. Shock capturing with PDE-based artificial viscosity for DGFEM: Part I. Formulation. *Journal of Computational Physics*, 229(5):1810–1827, March 2010.
- [3] A. Bonfiglioli, R. Paciorri, and L. Campoli. Unsteady shock-fitting for unstructured grids. *International Journal for Numerical Methods in Fluids*, 81(4):245–261, 2016.
- [4] L. Campoli, A. Assonitis, M. Ciallella, R. Paciorri, A. Bonfiglioli, and M. Ricchiuto. UnDiFi-2D: An unstructured discontinuity fitting code for 2D grids. *Computer Physics Communications*, 271:108202, 2022.
- [5] Graham Candler, Dimitri Mavriplis, and Loretta Trevino. Current Status and Future Prospects for the Numerical Simulation of Hypersonic Flows. In *47th AIAA Aerospace Sciences Meeting including The New Horizons Forum and Aerospace Exposition*, Orlando, Florida, January 2009. American Institute of Aeronautics and Astronautics.
- [6] Graham V. Candler, Michael Barnhardt, Travis Drayna, Ioannis Nompelis, David Peterson, and Pramod Subbareddy. Unstructured grid approaches for accurate aeroheating simulations. In *18th AIAA Computational Fluid Dynamics Conference*, Miami, Florida, June 2007. AIAA Paper 2006-3959.
- [7] Graham V. Candler, Pramod K. Subbareddy, and Joseph M. Brock. Advances in computational fluid dynamics methods for hypersonic flows. *Journal of Spacecraft and Rockets*, 52(1):17–28, January 2015.
- [8] Eric J. Ching, Yu Lv, Peter Gnoffo, Michael Barnhardt, and Matthias Ihme. Shock capturing for discontinuous Galerkin methods with application to predicting heat transfer in hypersonic flows. *Journal of Computational Physics*, 376:54–75, January 2019.
- [9] Mirco Ciallella, Mario Ricchiuto, Renato Paciorri, and Aldo Bonfiglioli. Extrapolated Shock Tracking: Bridging shock-fitting and embedded boundary methods. *Journal of Computational Physics*, 412:109440, July 2020.
- [10] Mirco Ciallella, Mario Ricchiuto, Renato Paciorri, and Aldo Bonfiglioli. Extrapolated discontinuity tracking for complex 2D shock interactions. *Computer Methods in Applied Mechanics and Engineering*, 391:114543, 2022.
- [11] Bernardo Cockburn and Chi-Wang Shu. Runge–Kutta discontinuous Galerkin methods for convection-dominated problems. *Journal of Scientific Computing*, 16(3):173–261, September 2001.
- [12] Andrew T. Corrigan, Andrew Kercher, and David A. Kessler. The Moving Discontinuous Galerkin Method with Interface Condition Enforcement for unsteady three-dimensional flows. In *AIAA Scitech 2019 Forum*.
- [13] Andrew T. Corrigan, Andrew D. Kercher, Pierson T. Guthrey, and Robert Nourgaliev. Application of mdg-ice to shock-material interface interactions. In *AIAA AVIATION 2021 FORUM*.
- [14] Andrew T. Corrigan, Andrew D. Kercher, and David A. Kessler. A moving discontinuous Galerkin finite element method for flows with interfaces. *International Journal for Numerical Methods in Fluids*, 89(9):362–406, 2019.
- [15] Andrew T. Corrigan, Andrew D. Kercher, David A. Kessler, and Devon A. Wood-Thomas. Convergence of the Moving Discontinuous Galerkin Method with Interface Condition Enforcement in the presence of an attached curved shock. In *AIAA Aviation 2019 Forum*.
- [16] Luke M. D’Aquila, Brian T. Helenbrook, and Alireza Mazaheri. A novel stabilization method for high-order shock fitting with finite element methods. *Journal of Computational Physics*, 430:110096, April 2021.

- [17] Pablo Fernandez, Cuong Nguyen, and Jaime Peraire. A physics-based shock capturing method for unsteady laminar and turbulent flows. Kissimmee, Florida, January January 2018. AIAA Paper 2018-0062.
- [18] Markus Geisenhofer, Florian Kummer, and Martin Oberlack. An extended discontinuous Galerkin method for high-order shock-fitting. *arXiv:2012.08860 [physics]*, December 2020.
- [19] Peter Gnoffo. Computational fluid dynamic technology for hypersonic applications. In *AIAA International Air and Space Symposium and Exposition: The Next 100 Years*, Dayton, Ohio, July 2003. AIAA Paper 2003-2829.
- [20] Peter Gnoffo. Multi-dimensional inviscid flux reconstruction for simulation of hypersonic heating on tetrahedral grids. In *47th AIAA Aerospace Sciences Meeting including The New Horizons Forum and Aerospace Exposition*, Orlando, Florida, January 2009. AIAA Paper 2009-599.
- [21] Ami Harten, Bjorn Engquist, Stanley Osher, and Sukumar R Chakravarthy. Uniformly high order accurate essentially non-oscillatory schemes, III. *Journal of Computational Physics*, 71(2):231–303, August 1987.
- [22] Tianci Huang and Matthew J. Zahr. High-order implicit shock tracking with targeted mesh optimization and pde-based smoothing. In *AIAA AVIATION 2021 FORUM*.
- [23] Tianci Huang and Matthew J. Zahr. A robust, high-order implicit shock tracking method for simulation of complex, high-speed flows. *Journal of Computational Physics*, 454:110981, 2022.
- [24] Guang-Shan Jiang and Chi-Wang Shu. Efficient implementation of weighted ENO schemes. *Journal of Computational Physics*, 126(1):202–228, June 1996.
- [25] Andrew D. Kercher and Andrew Corrigan. A least-squares formulation of the Moving Discontinuous Galerkin Finite Element Method with Interface Condition Enforcement. *Computers & Mathematics with Applications*, pages 1490–1519, November 2020.
- [26] Andrew D. Kercher, Andrew Corrigan, and David A. Kessler. The moving discontinuous Galerkin finite element method with interface condition enforcement for compressible viscous flows. *International Journal for Numerical Methods in Fluids*, 93(5):1490–1519, 2021.
- [27] Drew Kouri, Matthias Heinkenschloss, Denis Ridzal, and Bart van Bloemen Waanders. Inexact objective function evaluations in a trust-region algorithm for PDE-constrained optimization under uncertainty. *SIAM Journal on Scientific Computing*, 36(6):A3011–A3029, 2014.
- [28] Jaejin Lee, Manuel Huerta, and Gecheng Zha. Hypersonic 3-D blunt body equilibrium air flow using high order WENO schemes. In *41st Plasmadynamics and Lasers Conference*, Chicago, Illinois, June 2010. AIAA Paper 2010-4765.
- [29] Theodore Kai Lee and Xiaolin Zhong. Spurious numerical oscillations in simulation of supersonic flows using shock-capturing schemes. *AIAA Journal*, 37(3):313–319, March 1999.
- [30] Xu-Dong Liu, Stanley Osher, and Tony Chan. Weighted essentially non-oscillatory schemes. *Journal of Computational Physics*, 115(1):200–212, November 1994.
- [31] G. Moretti. Thirty-six years of shock fitting. *Computers & Fluids*, 31(4-7):719–723, 2002.
- [32] JOSEPH OLEJNICZAK, MICHAEL J. WRIGHT, and GRAHAM V. CANDLER. Numerical study of inviscid shock interactions on double-wedge geometries. *Journal of Fluid Mechanics*, 352:1–25, 1997.
- [33] Per-Olof Persson and Jaime Peraire. Sub-cell shock capturing for discontinuous Galerkin methods. AIAA Paper 2006-112, January 2006.
- [34] M.D. Salas. *A Shock-Fitting Primer*. CRC Press, 2009.

- [35] Yiqing Shen, Gecheng Zha, and Manuel Huerta. Simulation of hypersonic shock-wave/boundary-layer interaction using high order WENO scheme. In *48th AIAA Aerospace Sciences Meeting Including the New Horizons Forum and Aerospace Exposition*, Orlando, Florida, January 2010. AIAA Paper 2010-1047.
- [36] A. Shi, P.-O. Persson, and M.J. Zahr. Implicit shock tracking for unsteady flows by the method of lines. *Journal of Computational Physics*, 454:110906, 2022.
- [37] Bram Van Leer. Towards the ultimate conservative difference scheme. V. A second-order sequel to Godunov’s method. *Journal of Computational Physics*, 32(1):101–136, 1979.
- [38] Paul Woodward and Phillip Colella. The numerical simulation of two-dimensional fluid flow with strong shocks. *Journal of computational physics*, 54(1):115–173, 1984.
- [39] Jian Yu and Jan S. Hesthaven. A study of several artificial viscosity models within the discontinuous Galerkin framework. *Communications in Computational Physics*, 27(5):1309–1343, 2020.
- [40] Matthew J. Zahr and Per-Olof Persson. An optimization-based approach for high-order accurate discretization of conservation laws with discontinuous solutions. *Journal of Computational Physics*, 365:105–134, July 2018.
- [41] Matthew J. Zahr and Joseph M. Powers. High-order resolution of multidimensional compressible reactive flow using implicit shock tracking. *AIAA Journal*, 59(1):150–164, December 2020.
- [42] Matthew J. Zahr, Andrew Shi, and Per-Olof Persson. Implicit shock tracking using an optimization-based high-order discontinuous Galerkin method. *Journal of Computational Physics*, 410:109385, June 2020.
- [43] Dongyang Zou, Aldo Bonfiglioli, Renato Paciorri, and Jun Liu. An embedded shock-fitting technique on unstructured dynamic grids. *Computers & Fluids*, 218:104847, 2021.